energies

MDPI

Article

Integrated Phase-Change Materials in a Hybrid Windcatcher Ventilation System

Olamide Eso *, Jo Darkwa and John Calautit

Department of Architecture and Built Environment, Faculty of Engineering, University of Nottingham, University Park Campus, Nottingham NG7 2RD, UK
* Correspondence: olamide.eso@nottingham.ac.uk

Abstract: Windcatchers are effective passive ventilation systems, but their inability to actively reduce and stabilize supply air temperatures reduces indoor cooling performance. This study addresses this limitation by integrating encapsulated phase-change material tubes (E-PCM-Ts) into a solar fan-assisted, multidirectional windcatcher. The novelty lies in the vertical placement of E-PCM-Ts within the windcatcher's airstreams, enhancing heat transfer and addressing challenges related to temperature stabilization and cooling. Using computational fluid dynamics (CFD) under hot outdoor conditions, the ventilation, cooling, and PCM thermal storage performance are evaluated based on two different E-PCM-T arrangements. Results showed a maximum air temperature drop of 2.28 °C at a wind speed of 1.88 m/s and wind angle of 0°. This offers an optimal temperature reduction that achieved a 6.5% reduction for up to 7 h of air temperature stabilization. Placing E-PCM-Ts in all airstreams improved the thermal storage performance of the windcatcher. A 50% increase in hybrid ventilation efficiency was also achieved when wind angles increased from 0° to 30°. Overall, the proposed system demonstrated superior performance compared to that of traditional windcatchers, delivering improved thermal energy storage and cooling efficiency and adequate hybrid ventilation with supply air velocities of 0.37–0.60 m/s.

Keywords: CFD; cooling; hybrid ventilation; phase-change material; thermal energy storage; multidirectional windcatcher

check for updates

Academic Editor: Antonio Lecuona

Received: 1 August 2024
Revised: 30 January 2025
Accepted: 2 February 2025
Published: 11 February 2025

Citation: Eso, O.; Darkwa, J.; Calautit, J. Integrated Phase-Change Materials in a Hybrid Windcatcher Ventilation System. *Energies* **2025**, *18*, 848. https://doi.org/10.3390/en18040848

1. Introduction

Buildings account for 40% of total energy consumption worldwide [1], with the use of heating, ventilation, and air conditioning (HVAC) systems being a major contributor to this high building energy demand globally [2]. HVAC systems consume 57% of end-use energy in commercial and residential buildings [3]. Since HVAC systems primarily run on electricity, and fossil fuels remain a dominant source of power generation globally, most of these systems are still heavily reliant on non-renewable energy. Moreover, many HVAC systems use refrigerants with high global warming potential (GWP) [4], significantly contributing to climate change. As a result, the cooling services industry accounts for over 10% of global greenhouse gas (GHG) emissions [5].

Traditional air conditioning (AC) alone accounts for 4% of these emissions, which are estimated to be twice as high as those produced by the entire aviation industry [6]. Consequently, researchers are actively exploring more sustainable and energy-efficient alternatives to traditional AC systems.

1.1. Windcatchers

Passive ventilation systems [7], such as windcatchers, offer greener alternatives to fossil fuel-powered AC [8]. Typically mounted on building roofs, windcatchers utilize prevailing winds and the stack effect to achieve effective ventilation [9].

Traditional windcatchers, also known as "badgirs", have been used for centuries in Middle Eastern buildings for passive ventilation [10]. Modern windcatcher designs, however, have evolved to meet the ventilation needs of urban buildings [11]. According to the existing literature, windcatchers are classified based on various parameters such as the number of vents, internal partitions, stores, or cross-sectional structures [12]. However, depending on the number of vents, the most typical descriptors are unidirectional (one-sided), two-sided, or multidirectional. Windcatchers in the multidirectional family can be either four-sided, six-sided, eight-sided, or circular [13].

1.2. Multidirectional Windcatcher Passive Ventilation

Multidirectional windcatchers are more suitable for building ventilation in hot climates with low wind conditions [14]. For instance, Jafari et al. [2] implemented a combination of a multidirectional windcatcher, a solar chimney, and water spray to address the limitation of no-wind conditions for indoor thermal comfort. Further studies indicate that, compared to equivalent single-sided window openings in similarly sized buildings, multidirectional windcatchers can achieve higher indoor air exchange efficiency due to the vents' multidirectional design [15]. Li and Mak [16] compared the use of multidirectional windcatchers and equivalent-sized single-sided window openings in similar-sized buildings. Results suggested that the multidirectional windcatcher offered 0.33–0.39 m/s more indoor airflow in the building than the equivalent single-sided window opening. Figure 1 graphically illustrates how a roof-mounted multidirectional windcatcher system generates a more effective indoor airflow pattern compared to that of an installed single-window setup in a similarly sized space.

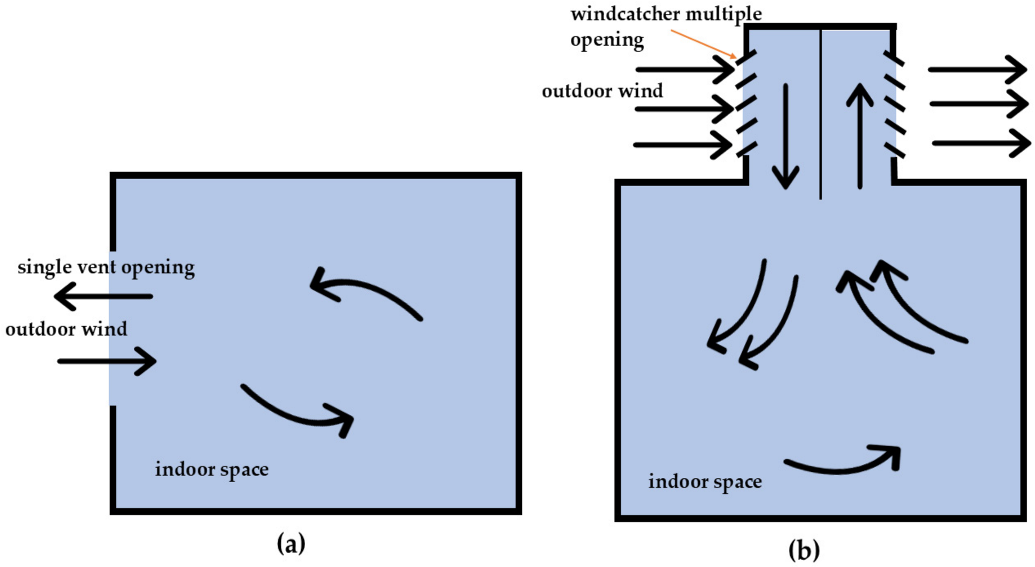

Figure 1. Comparison of airflow patterns between single-window opening and top-mounted windcatcher with multiple openings. (**a**) represents a room ventilated with a single vent opening (without windcatcher). (**b**) represents a room ventilated with a multidirectional windcatcher.

A typical four-sided multidirectional windcatcher is divided into quadrants by an X-shaped partition, as shown in Figure 2 [17]. These quadrants play specific roles in the airflow ventilation operation, with one quadrant typically supplying fresh air, while the other three quadrants expel air out of the ventilated space. However, the airflow dynamics can change slightly depending on the angle of the prevalent leeward wind incident to the windcatcher. However, in principle, the effectiveness of the windcatcher airflow primarily relies on parameters such as wind speed, wind direction, differences in indoor–outdoor air pressure, and air temperature variance [18]. These parameters are commonly monitored in windcatcher studies, which typically use small-scale and full-scale experiments, as well as theoretical assessments based on analytical, empirical, and numerical modeling techniques [19]. These techniques also provide a robust foundation for evaluating windcatcher performance, which has predominantly focused on ventilation and cooling effectiveness in recent years. Table 1 summarizes key studies on windcatchers from the past five years, highlighting their design variations, operational limitations, and research gaps.

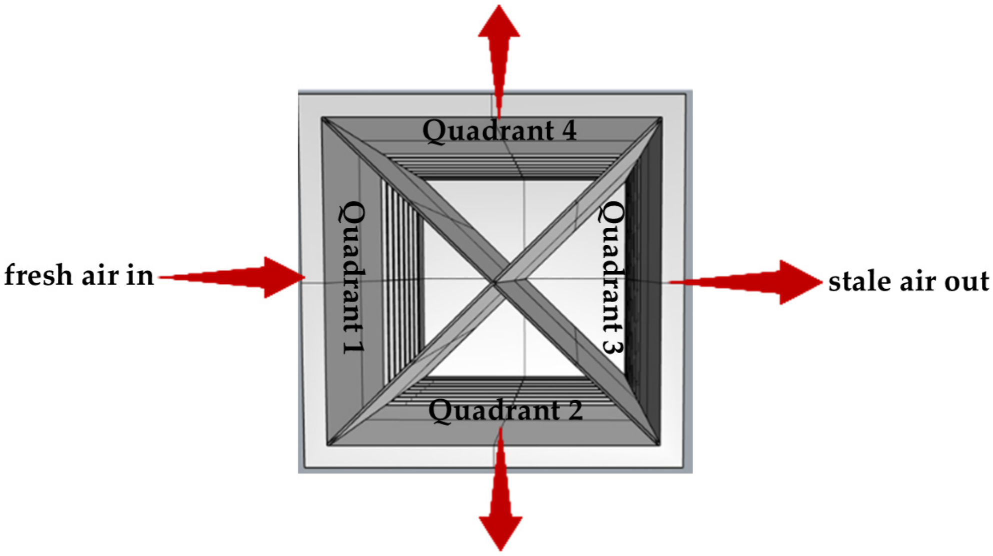

Figure 2. Cross-section of a four-sided multidirectional windcatcher showing airflow patterns through the X-shaped partitions/quadrants.

Table 1. Key studies on windcatcher ventilation and cooling performance studies, highlighting their design variations, operational limitations, and research gaps.

Ref.	Year	Study	Design Variation	Operational Limitations	Research Gaps
Ventilation performance					
[20]	2023	Experiment and numerical investigation of a novel flap fin louver windcatcher for multidirectional natural ventilation and passive technology integration.	Flap fins on inlet openings enable direction-independent ventilation.	Relies heavily on wind direction and speed; low performance in variable and low wind conditions.	Integration with passive cooling, heating, and dehumidification systems not explored.
[21]	2024	Parametric analysis of a novel rotary scoop dual-channel windcatcher for multidirectional natural ventilation of buildings.	Rotary scoop dual channel separates airflow.	Airflow leakage due to gaps in the bearing system, reducing ventilation performance.	Did not address the potential of incorporating assisted ventilation to enhance system performance in low wind conditions.

Table 1. *Cont.*

Ref.	Year	Study	Design Variation	Operational Limitations	Research Gaps
[22]	2024	Use of wind wall-integrated windcatcher.	Incorporated upper wing walls (UWWs) into a two-sided windcatcher.	Limited operation in turbulent and varied wind conditions.	Integration with passive cooling technologies not considered.
[23]	2020	Windcatcher louvers to improve ventilation efficiency.	Clark Y fixed airfoil-type louver with single-sided windcatcher.	Performance reduced in low or turbulent wind conditions.	Multidirectional windcatchers and wider climate adaptability not explored.
[2]	2021	Numerical simulation of natural ventilation with passive cooling by diagonal solar chimneys and windcatcher and water spray system in a hot and dry climate.	Combines windcatcher, three solar chimneys, and WSS.	Limited to hot, dry climates; feasibility of WSS in water-scarce areas not addressed.	Experimental validation missing.
[24]	2022	The effect of onset turbulent flows on ventilation with a two-sided rooftop windcatcher.	Assesses wind incidence angles for ventilation.	Relies on window opening for optimal operation.	Single-sided and multidirectional designs not explored and lacks computational validation.
Cooling performance					
[25]	2024	Radiative cooling ventilation improvement using an integrated system of windcatcher and solar chimney.	Solar chimney integrated with radiative cooling windcatcher.	Vent opening positioning for optimization not addressed; limited to hot, dry climates.	Performance in humid or mixed climates not assessed.
[26]	2023	Experimental and numerical evaluation of a novel dual-channel windcatcher with a rotary scoop for energy-saving technology integration.	The rotary scoop separated the supply and return ducts.	Performance depends on the outdoor wind, reducing reliability in variable conditions.	PCM integration not explored for placement, selection, and effectiveness in different climates.
[27]	2024	Optimizing Windcatcher Designs for Effective Passive Cooling Strategies in Vienna's Urban Environment.	Evaluated one-sided and two-sided windcatchers but does not explore multidirectional designs.	Does not address windcatcher performance in low or no wind conditions, crucial for areas with inconsistent winds.	Focused on Central European climates, not hot climates. Relied on DesignBuilder simulations without experimental, CFD, or real-world validation.

1.2.1. Effect of Wind Speeds on Windcatcher Ventilation

Higher wind speeds generally lead to increased ventilation rates in windcatchers [28]. However, excessively high wind speeds may not necessarily benefit windcatcher cooling performance. In general, multidirectional windcatchers offer more satisfactory ventilation in limited wind speed conditions than other types of windcatchers [14]. Gharakhani et al. [29] conducted wind tunnel experiments and CFD analysis to investigate windcatcher ventilation performance under low-wind hot conditions. They found that increasing the number of vents and optimizing windcatcher height improved ventilation at nominal wind speeds of 5–7 m/s.

Studies by Calautit et al. [30] and O'Connor et al. [31] demonstrated that four-sided multidirectional windcatchers could operate efficiently even at low wind speeds of 2 m/s, a capability attributed to the optimal sizing and placement of vents [32]. Similarly, Dehghani-Sanij et al. [33] investigated a single-sided rotating cylindrical windcatcher with moistened pads. Their findings indicated that greater ventilation efficiency was achieved at higher wind speeds, typically ranging from 3 to 10 m/s.

1.2.2. Effect of Wind Angles on Windcatcher Ventilation

Wind angle is a critical factor influencing pressure differences across the openings of passive ventilation systems, such as multidirectional windcatchers [34]. Research has shown that the highest ventilation efficiency and pressure coefficients are achieved when wind flows directly into the vents at a 0° angle [17]. However, as wind angles deviate incrementally, airflow rates decrease until ventilation becomes negligible [35]. Angles exceeding 45° significantly reduce cooling performance [26]. Afshin et al. [36] confirmed that zero-ventilation performance occurs at a wind angle of 55°.

Calautit et al. [37] conducted wind tunnel experiments and CFD simulations to evaluate the impact of wind angles on the performance of a four-sided multidirectional windcatcher. Using boundary conditions with wind speeds ranging from 0.5 to 5 m/s and wind angles between 0° and 90°, they found that the highest ventilation efficiency occurred at a wind angle of 45° with a wind speed of 3 m/s. This configuration resulted in an indoor volumetric flow rate of 0.47 m^3/s, which was 32% higher than the flow rate observed at a 0° wind angle.

These studies emphasize the significant influence of wind speed and angle on the passive ventilation potential of four-sided multidirectional windcatchers. Hybrid ventilation systems, which incorporate fans, have shown promise in mitigating the effects of varying wind angles on ventilation performance. However, the extent to which hybrid systems can address these challenges has not been comprehensively explored in the existing literature, warranting further investigation.

1.3. Fan-Assisted Windcatcher Hybrid Ventilation

Despite the improved ventilation potential of windcatchers, time-varying flows and irregular ventilation pose significant barriers to achieving optimal building ventilation performance [38]. Zhang et al. [39] suggested that adopting hybrid ventilation rather than passive ventilation can overcome these limitations. Several studies have demonstrated the potential of integrating fans into windcatchers to improve ventilation performance. For instance, Sangdeh and Nasrollahi [17] discussed the potential of incorporating fans with windcatchers to achieve hybrid ventilation. Hughes et al. [40] discussed the use of a low-energy fan incorporated at the top of a windcatcher and connected to solar panels to ensure continuous airflow when no outdoor wind is available.

Elmualim [41] explored the combination of a mechanical fan system with a windcatcher to enhance indoor airflow. However, the study did not verify the specific contribution of the windcatcher to the overall ventilation performance. Hughes and Ghani [42] developed a CFD model to evaluate the impact of different fan positions on windcatcher-induced airflow. Their results indicated a consistent ventilation rate of 370 L/s when the fan was positioned at the top of the windcatcher with a fan pressure of 20 Pa. This established the potential for hybrid systems to maintain ventilation throughout the day, even under low wind conditions.

Lavafpour and Surat [43] suggested orienting wall-mounted fans parallel to the windcatcher vents to reduce irregular ventilation flows. However, their study lacked supporting data, highlighting the need for further research on fan-assisted windcatchers to better understand hybrid ventilation optimization. While the ventilation effectiveness of hybrid windcatchers is evident, challenges remain. In alignment with the global emphasis on sustainable energy technologies, solar fans could serve as an alternative to mechanical fans in windcatchers. Hybrid multidirectional windcatcher systems show promise, but achieving efficient and stable cooling remains crucial for widespread application in hot climates [44]. This issue can be addressed by combining windcatchers with additional passive cooling strategies.

1.4. Integrating Passive Cooling Devices with Windcatchers

The integration of passive cooling systems into windcatchers has been widely discussed in the literature [45], with previous studies using both experimental [46] and numerical analyses [44]. Recently, significant attention has been given to the integration of heat pipes to enhance windcatcher cooling performance. However, as discussed below, heat pipes come with specific limitations that must be addressed.

1.4.1. Heat Pipe Integration with Windcatchers

Heat pipes are effective, low-energy heat transfer devices that can significantly reduce incoming air temperatures when integrated with windcatchers [47]. Calautit et al. [47] reported that heat pipes exhibit a sensible effectiveness of 45–65%. In one study, heat pipes were incorporated into a unidirectional windcatcher to assess cooling performance across varying wind speeds (1–5 m/s) [48]. Results showed a reduction in supply air temperature by 9.5–12 °C, with better cooling performance observed at lower wind speeds (1–2 m/s) than at higher wind speeds (5 m/s).

In another study, Calautit et al. [30] investigated cylindrical heat pipes in a unidirectional windcatcher under an external air temperature of 318 K. This configuration achieved a 12 K reduction in supply air temperature. Although ventilation rates decreased by 20–35% due to the internal heat pipe arrangement, the system maintained an airflow rate of up to 10 L/s per person. The authors suggested that fan integration could further improve ventilation rates, reaffirming the cooling efficacy of heat pipes.

A numerical study by Calautit et al. [47] compared the integration of evaporative cooling and heat pipes into a commercial windcatcher. Both systems achieved comparable temperature drops of up to 15 °C. However, heat pipes were favored due to their ability to conserve water, even though both approaches required working fluids (water or ethanol) for consistent cooling. Nevertheless, these studies did not address the inability of windcatchers to consistently stabilize supply air temperatures, a challenge that PCMs could potentially overcome.

1.4.2. PCMs—Thermal Energy Storage Integration with Windcatchers

PCMs are highly effective for thermal energy storage due to their substantial latent heat capacity, which allows for significant cooling load shifts from peak to off-peak periods [49]. PCMs can absorb and release latent heat with minimal temperature variation, enabling the reduction in and stabilization of air temperatures for effective passive cooling [50,51].

O'Connor et al. [52] demonstrated that PCM integration in ventilation systems is feasible, as PCMs exert minimal impact on airflow pressure. Despite limited research on PCM integration into windcatchers, the results of existing studies suggest significant potential. For instance, Seidabadi et al. [53] conducted a heat transfer study using MATLAB software on a two-sided windcatcher integrated with PCMs. However, the authors first developed the model as a two-dimensional (2D) model and later extended to three-dimensional (3D) model. The heat and mass transfer codes were developed in MATLAB using the PDSIMUL time-dependent function to solve the differential equations for PCM phase change and energy balance. These calculations were then integrated with the Finite Element Method (FEM) to simulate PCM behavior and airflow dynamics. Overall, the system achieved a

15 K reduction in air temperature and maintained temperature stability for 7 h, although heat transfer efficiency was reduced due to the PCM's placement within the windcatcher walls.

Lizana et al. [54] improved air–PCM heat transfer by integrating PCMs directly into the airstream of a ventilated cooling ceiling. Similarly, Rouault et al. [55] found that the shape and arrangement of PCM profiles within a latent heat thermal energy storage (LHTES) ventilation system strongly influenced heat transfer and melting performance. Abdo et al. [56] reported a 9.85% temperature reduction (2.78 °C) when PCMs were placed directly within the airstream of a two-sided windcatcher.

Despite these promising findings, research on the thermal energy storage performance of multidirectional windcatchers remains scarce.

1.5. Gap in Knowledge, Novelty, and Aims

The studies discussed clearly show that the potential to enhance windcatcher ventilation has been thoroughly explored. Recent research has also focused on enhancing the cooling performance of windcatchers, with heat pipes playing a prominent role in these studies.

Some investigations have explored the use of heat pipes with cold-water storage for unidirectional (one-sided) windcatcher cooling [17,18], while others have examined heat pipes in two-sided windcatcher configurations [57]. However, a significant drawback of these systems is the need for continuous water replacement in the storage tanks to ensure effective heat transfer. In contrast, PCMs offer a more streamlined system configuration while improving windcatcher cooling and thermal energy storage performance. Essentially, PCMs serve a dual function as both heat transfer devices and heat sinks.

The existing literature highlights that PCMs have a substantial latent heat storage capacity [58], with minimal temperature fluctuations during phase transitions [59]. This capability enables the shifting of peak cooling loads to off-peak periods [51], which can be advantageous for enhancing windcatcher cooling and thermal energy storage. Despite these benefits, there is a limited understanding of how PCMs can be integrated into windcatcher systems. In particular, the effect of incorporating encapsulated PCMs into multidirectional windcatchers, especially those designed for hybrid ventilation, remains underexplored. Furthermore, the impact of wind speed on the thermal energy storage performance of hybrid multidirectional windcatcher systems also remains poorly understood, underscoring the need for further investigation. This gap raises several key research questions:

- How can encapsulated PCMs be optimally integrated into hybrid multidirectional windcatchers to improve both cooling and thermal energy storage performance without compromising overall ventilation effectiveness?
- What influence will variations in wind speed and angle have on the system's cooling, thermal energy storage, and overall ventilation performance?

To address these questions and overcome the cooling and thermal energy storage deficiencies of traditional windcatchers, this study introduces a novel solar fan-assisted multidirectional windcatcher that incorporates encapsulated PCM tubes (E-PCM-Ts) directly within its airstreams. The system's novelty lies in the vertical integration of E-PCM-Ts within the airstreams, enhancing heat transfer and addressing temperature stabilization challenges. Additionally, the use of a wall-mounted solar fan, rather than a roof-mounted one, effectively reduces the airflow resistance caused by PCMs, functioning as a secondary airflow vent.

This study aims to assess the feasibility of integrating E-PCM-Ts as a cooling and thermal energy storage solution for multidirectional windcatchers without compromising ventilation performance. To achieve this, this study evaluates the impact of wind speeds, wind angles, and different E-PCM-T configurations on the system's thermal energy storage, cooling performance, and ventilation effectiveness. A numerical analytical approach based on validated computational fluid dynamics (CFD) models was employed. The windcatcher model's ventilation performance was validated initially, followed by validation of the E-PCM-T thermal energy storage performance. Finally, the integrated hybrid system with E-PCM-Ts was thoroughly assessed.

2. Methods

2.1. Proposed System

As illustrated in Figure 3, the proposed system incorporates encapsulated phase-change material tubes (E-PCM-Ts) within a solar fan-assisted multidirectional windcatcher. The X-shaped partition divides the windcatcher airstreams into four quadrants, preventing crossflow within the system. A wall-mounted axial solar fan ensures hybrid ventilation by minimizing airflow fluctuations and reducing resistance caused by the E-PCM-Ts within the airstreams.

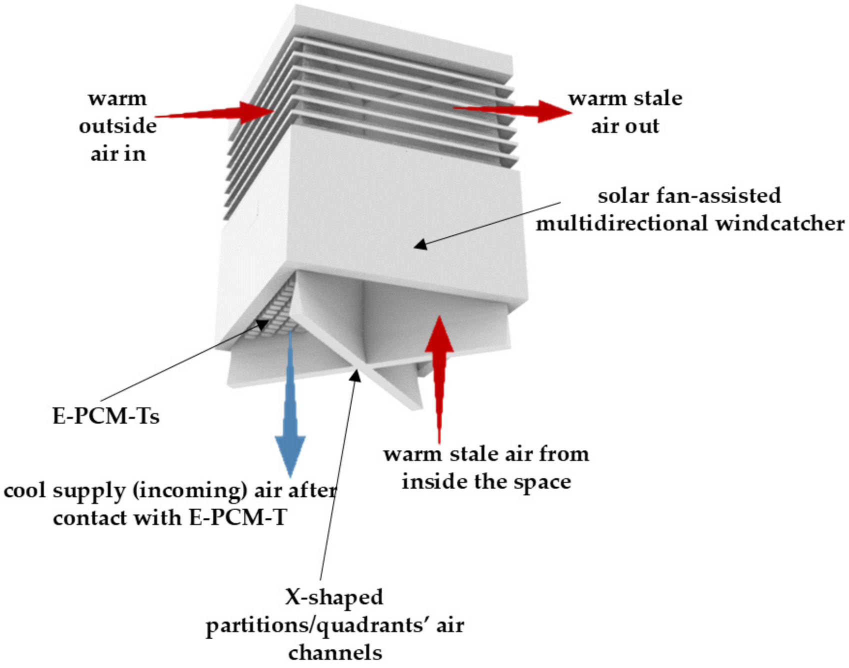

Figure 3. The hybrid multidirectional windcatcher system with E-PCM-Ts.

To investigate the impact of E-PCM-T inclusion in the windcatcher, two distinct arrangements of E-PCM-Ts were proposed. In the first arrangement (Case 1), as shown in Figure 4, the windcatcher was integrated with 48 E-PCM-Ts placed solely within the supply airstream. In the second arrangement (Case 2), 48 E-PCM-Ts were placed in each of the four windcatcher airstreams, resulting in a total of 197 E-PCM-Ts evenly distributed across all quadrants.

The operation of the proposed system relies on three simultaneous processes: airflow, thermal energy storage, and air cooling. As illustrated in Figure 5, warm outdoor air enters through the windward vents of the windcatcher and passes directly over the E-PCM-Ts in the supply airstreams. This direct interaction facilitates efficient heat transfer, allowing the E-PCM-Ts to absorb and store heat from the incoming air. Consequently, the supply air temperature (T_S) is effectively reduced before being delivered into the ventilated space. Simultaneously, as cooling occurs in the supply airstream, stale and warm air is expelled from the ventilated room through the exhaust vents located on the leeward side of the windcatcher [17].

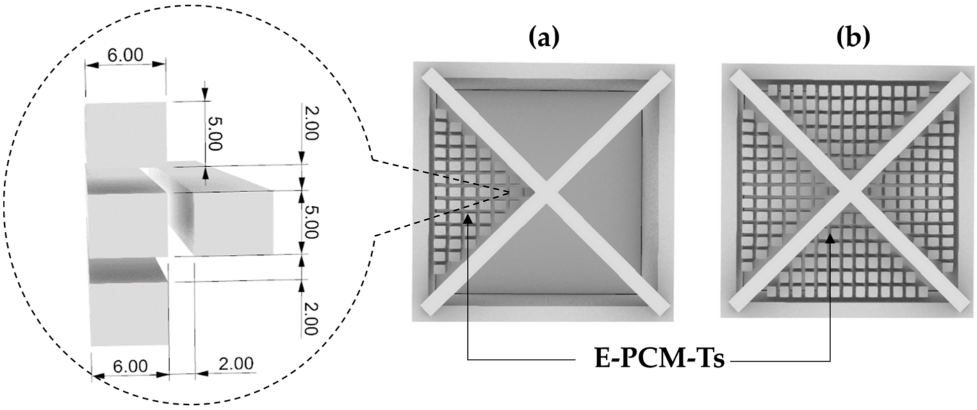

Figure 4. Two different arrangements of the E-PCM-Ts within the integrated windcatcher airstreams. (**a**) represents Case 1, incorporating 48 E-PCM-Ts within a single supply airstream. (**b**) represents Case 2, incorporating 197 E-PCM-Ts evenly distributed across all four airstreams.

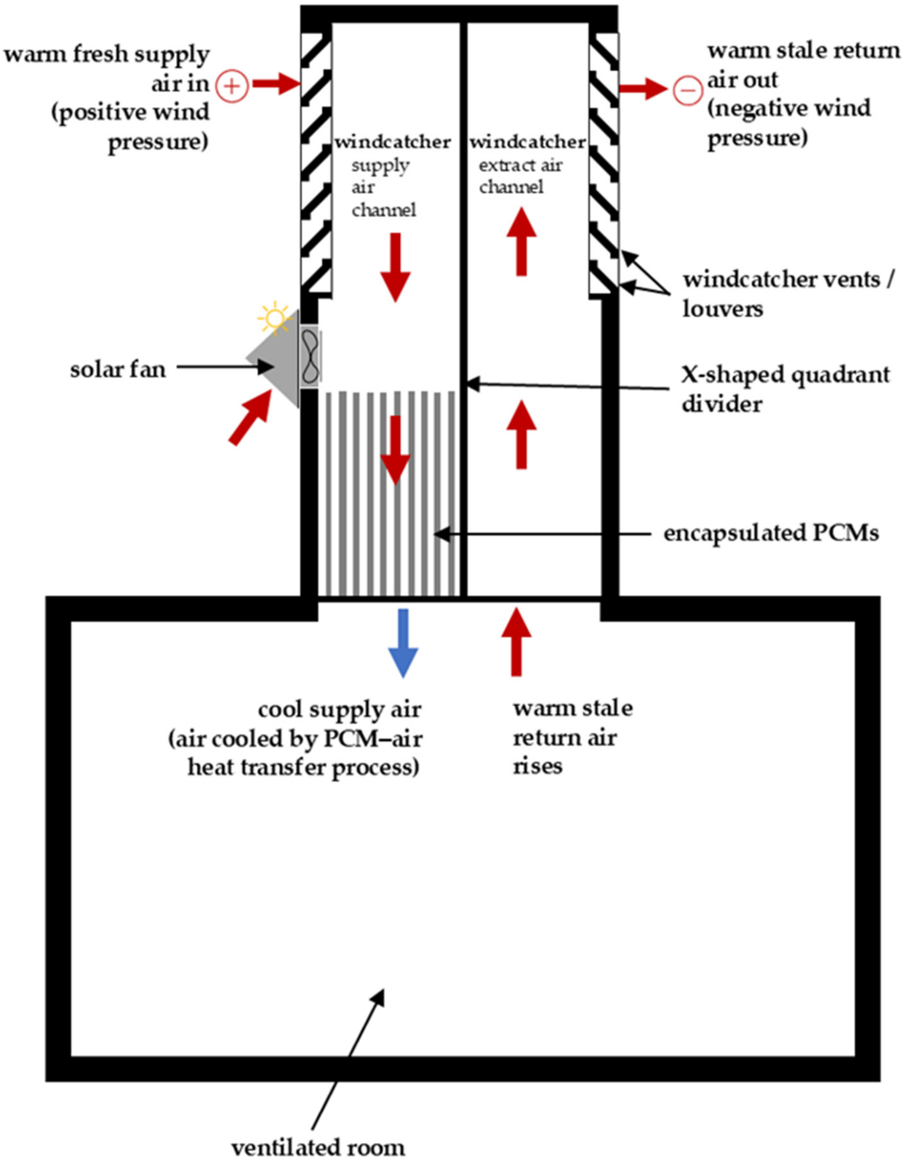

Figure 5. Airflow and cooling process in the hybrid windcatcher system.

2.2. Geometry and Computational Domain

The 3D geometry of the proposed system was initially developed using Rhino 6 CAD software and then refined into a simplified computational model using the ANSYS 18.0 Design Modeler within the ANSYS Workbench environment. The fluid volume of the model was extracted from the solid model to simplify the physical domain for computational simulation. As shown in Figure 6, the computational domain includes the macroclimate (representing the outdoor airflow domain), the solar fan-assisted multidirectional windcatcher integrated with E-PCM-Ts, and the microclimate (representing the single-zone ventilated room). To prevent reverse flow within the macroclimate domain, the far-field pressure outlet was extended 20 m from the inlet boundary.

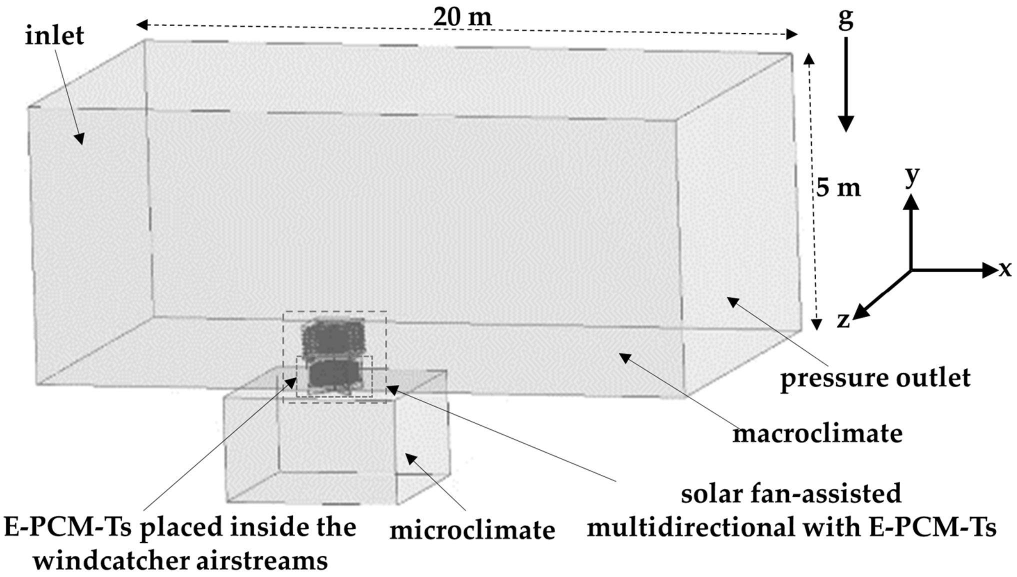

Figure 6. Computational domain and boundary conditions.

2.3. Material Selection

The optimal PCM melting temperature, $T_{m,r}$, for the set average room temperature, $\overline{T}_r$, was derived from Equations (1) and (2), based on the studies by Peippo et al. [60] and Nazir et al. [61]. As a result, RT28HC paraffin, a commercially available Rubitherm GmbH PCM product with a melting temperature of 28 °C (301.15 K) and a solid-state specific heat capacity of 1650 $J/kg\ K^{-1}$ was selected [55].

$$T_{m,r} = \overline{T}_r + \frac{Q}{h \times t_s} \tag{1}$$

where Q represents the absorbed heat in a room per unit area surface in Jm^{-2}, stored based on a diurnal storage cycle, and $t_s = t_c + t_d$. The wall surface heat transfer coefficient is given as h in $Wm^{-2}\ K^{-1}$.

$$\overline{T}_r = \frac{t_c T_d + t_d T_n}{t_c + t_d} \tag{2}$$

where T_d represents the daytime room temperature, and T_n represents the nighttime room temperature based on the PCM charging (t_c) and discharging (t_d) times.

This choice aligns with the recommended thermo-properties for PCMs suitable for hot outdoor conditions, as specified in the studies by Sheriyev et al. [62] and Lei et al. [63]. For this study, the selected PCM was encapsulated in rectangular aluminum tubes measuring 50 × 60 × 500 mm, with a conduction thickness of 0.001 mm. The thermophysical properties of the PCM and its encapsulation material, aluminum, are presented in Table 2.

Table 2. Thermophysical properties of RT28HC PCM encapsulated in aluminum tube [55,64]. s—PCM in solid state, l—PCM in liquid state.

Properties	PCM (RT28 HC)	Aluminum Encapsulation Material (Al)
Melting temperature (K)	301.15	-
Temperature (K)	300.15 (s), 302.15 (l)	-
Specific heat capacity (J/kg K^{-1})	1650 (s), 2200 (l)	910
Density (kg/m^3)	880 (s), 768 (l)	2719
Thermal conductivity (W/m K^{-1})	0.2	-
Dynamic viscosity (kg/m s)	0.00238	-
Latent heat (J/kg)	245,000	-
Melting volume expansion (%)	14	-
Kinematic viscosity (mm/s)		3.1×10^{-6}

The PCM mass for a single E-PCM-T based on its volume and density was calculated using Equation (3):

$$V_{PCM,tube} = W_t \times H_t \cdot L_t \cdot l_f \tag{3}$$

where W_t is the tube width, H_t is the tube height, tube length is L_t, and l_f is the PCM volume fraction (default value is 1, assuming PCM completely fills the tube).

PCM mass for a single E-PCM-T is calculated using Equation (4):

$$m_{PCM,total} = V_{PCM,tube} \cdot \rho_{PCM} \tag{4}$$

PCM mass for N E-PCM-Ts scaled across the system was calculated using the following:

$$m_{PCM,total} = m_{PCM,tube} \cdot N \tag{5}$$

Accordingly, PCM volume per E-PCM-T was 0.0015 m^3, with a mass of 1.32 kg. The total PCM in Case 1 was 63.36 kg (15.52 MJ energy storage) and in Case 2, 260.04 kg (63.61 MJ energy storage). Despite its large mass, the PCM offers a high energy storage per unit volume offering a better energy density solution that requires significantly less weight than that of other traditional thermal storage materials like concrete or water [65] to store the same energy.

2.4. CFD Numerical Modeling

Numerical modeling was performed using Ansys Fluent 18.0 CFD software. The transient 3D RANS (Reynolds-Averaged Navier–Stokes) with standard k–ε turbulence model was adopted to simulate the airflow. The turbulence intensity at the windward inlet of the flow domain was assumed to be 5%, and the turbulent viscosity ratio was assumed to be 10, consistent with the CFD methodology outlined by [40]. The Finite Volume Method (FVM) and Semi-Implicit Method for Pressure-Linked Equations (SIMPLE) were employed to solve the governing equations without any modifications, as described by [66].

As indicated in Figure 7, twelve monitoring points were created in the CFD model to monitor all properties throughout the numerical simulation aligned with the vector points in Calautit et al.'s experimental model [35]. The PCM phase transition and heat transfer problem were solved using the numerical algorithm for the "Stefan problem" during the simulation exercise discussed in Prakash et al.'s study [67].

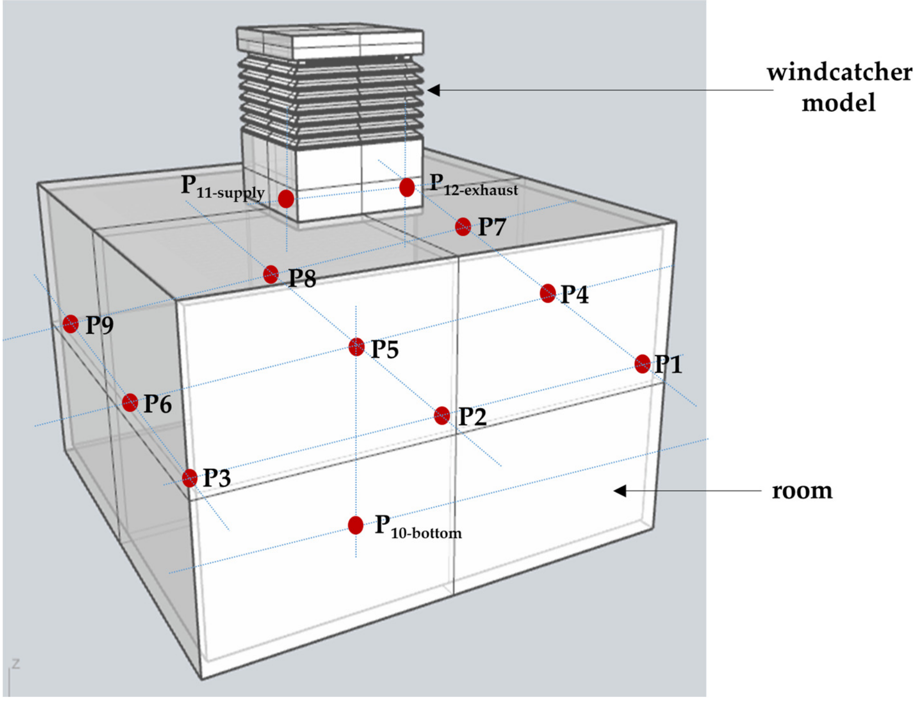

Figure 7. The twelve monitored points where readings were taken throughout the windcatcher simulation study.

2.4.1. Assumptions

The following assumptions were adopted during the numerical simulation:

- The initial temperature of the PCM was set at 293 K (20 °C).
- Volume expansion of the PCM during phase change was neglected in the solution computation.
- The PCM was considered isotropic, with uniform thermal conductivity.
- All thermophysical properties were assumed to be homogenous and constant, independent of temperature variations.
- Convective heat loss around the windcatcher and room walls was neglected, assuming adiabatic conditions.
- Airflow in the model was assumed to be incompressible, transient, and turbulent.

2.4.2. Governing Equations

Based on the assumptions stated in Section 2.4.1, the model's airflow physical behavior and the PCM–air heat transfer interfaces are governed by Equations (6)–(14) in Section Governing Equations for the Airflow Within the Model and Section Governing Equations for the PCM Phase Transition Heat Transfer Interfaces, respectively.

Governing Equations for the Airflow Within the Model

Within the k-ε turbulence model, airflow transport is governed by the conservation equations for mass, momentum, and energy, which are fundamental in describing all turbulence model transport phenomena.

Conservation of mass:

$$\frac{\delta \rho}{\delta t_j} + \frac{\delta}{\delta t}(\rho u_i) = 0 \tag{6}$$

where the fluid velocity in the model is represented by u, the density of air is represented by ρ, and time is t.

Momentum conservation:

$$\frac{\partial(\rho u)}{\partial t} + \nabla\cdot(\rho u u) = -\nabla p + \rho g + \nabla\cdot(\mu \nabla u) - \nabla\cdot\tau_t \tag{7}$$

The vectors in the equations are represented as p, pressure, and g, gravitational acceleration. The molecular dynamic viscosity is represented as μ; τ_t represents the turbulence stress divergence that occurs due to the velocity fluctuations caused by the auxiliary stresses in the model.

Energy conservation:

$$\frac{\partial(\rho e)}{\partial t} + \nabla\cdot(\rho e u) = \nabla\cdot(k_{eff}\nabla T) - \nabla\cdot\left(\sum_i h_i j_i\right) \tag{8}$$

where e represents specific internal energy and effective heat conductivity, k_{eff}; the temperature of the air is represented by T; and h_i represents the fluid-specific enthalpy while j_i is the mass flux.

Turbulent kinetic energy:

$$\frac{\partial(\rho k)}{\partial t} + \nabla\cdot(\rho k u) = \nabla\cdot[\alpha_k k_{eff} \nabla k] + G_k + G_b - \rho_\epsilon \tag{9}$$

G_k is the TKE source caused by the average velocity gradient; G_b represents the TKE source based on buoyancy force; the turbulent Prandtl constants are represented by constants α_k and α_ε; and vectors $C_{1\varepsilon}$, $C_{2\varepsilon}$, and $C_{3\varepsilon}$ are the empirical model constants.

Energy dissipation rate:

$$\frac{\partial}{\partial t}(\rho Y_i) + \nabla\cdot(\rho u Y_i) = -\nabla\cdot\vec{J_i} + R_i + S_i \tag{10}$$

where $\vec{J_i}$ represents the fusion flux of species i, R_i represents the net rate of production of species I, and S_i is the rate of creating species by addition from the dispersed phase and any user-defined sources.

Governing Equations for the PCM Phase Transition Heat Transfer Interfaces

The PCM was modeled based on the Stefan problem using the temperature method. Hence, the equations solve the temperature distribution and phase change that occur within the PCM. By tracking temperature as a key variable, this method effectively represents the heat transfer and thermal conductivity behavior of the PCM during its phase change. It avoids the need to delve into intricate fluid dynamics details, phase-change interfaces, or complex multiphysics interactions within the PCM, thus reducing computational resource demands and balancing the CFD modeling complexity and the accuracy of the result. Based on this, the PCM temperature variation and melting phase transition in the 3D model are described using continuity Equations (11) and (12) for melting and solidification, along with momentum Equation (13) [68].

$$\nabla\cdot\vec{\mathcal{U}} = 0 \tag{11}$$

$$\text{where } \mathcal{U} \text{ is the 3D velocity vector}: \vec{\mathcal{U}} = (\mathcal{U}_x, \mathcal{U}_y, \mathcal{U}_z). \tag{12}$$

$$\rho_f\left(\frac{\partial\vec{u}}{\partial t} + \vec{u}\cdot\nabla\vec{u}\right) = -\nabla p + \mu_f \nabla^2\vec{u} + \rho_f \vec{g}\beta(T_f - T_m) + \frac{C(1-f_l)^2}{S + f_l^{\,3}}\vec{u} \tag{13}$$

where β is the thermal expansion coefficient (1/K), the simulation coefficients are represented by S and C, while the PCM liquid fraction is represented by f_l. g is the gravitational acceleration vector. T_f is the fluid temperature and T_m is the melting temperature.

Furthermore, the PCM liquid fraction, f_l, during the simulation is given by Equation (10). f_l is a function of T temperature which is applied across the 3D temperature field. The T_s PCM temperature in a solid state is 300.15 K (27 °C) and the T_l PCM temperature in a liquid state is 301.15 K (29 °C).

$$f_l = \begin{cases} 0 & T < T_s \\ \frac{T-T_s}{T_l-T_s} & T_s < T < T_l \\ 1 & T > T_l \end{cases} \tag{14}$$

2.4.3. Mesh Generation and Adaptation

Two non-uniform hybrid computational meshes were generated for the Case 1 and Case 2 models. As shown in Figure 8, the regions around the E-PCM-Ts were refined using face meshing techniques to achieve higher mesh density in critical areas. This refinement was essential to accurately resolve the airflow and heat transfer phenomenon. It was particularly focused on the region circled in red in Figure 8, where steep temperature and velocity gradients were anticipated to occur. By enhancing the mesh resolution in these zones, the simulations provided more precise predictions of heat transfer rates and airflow behavior. This targeted meshing strategy effectively captured the complex thermal and fluid interactions within the E-PCM-T region, offering deeper insights into the modeling intricacies. A grid sensitivity analysis, discussed in Section 2.4.4, ensured that the error in the posterior estimate was negligible.

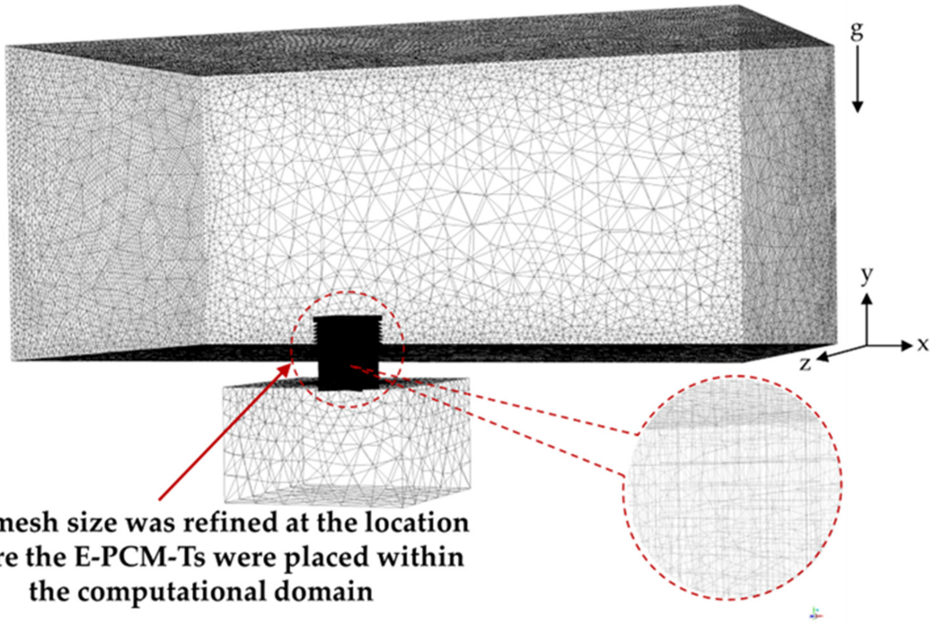

The mesh size was refined at the location where the E-PCM-Ts were placed within the computational domain

Figure 8. The computational grid is based on a non-uniform hybrid mesh.

2.4.4. Grid Sensitivity Analysis

A grid sensitivity analysis was performed to ensure an insignificant posterior estimate error by systematically varying the mesh size from coarse to fine grids [69]. As presented in Table 3, the mesh sizes ranged from 4.6 million to 14.5 million elements. The fine mesh for the Case 1 model, which included 11.6 million elements and 2.2 million nodes, and the Case 2 model, with 14.5 million elements and 2.8 million nodes, exhibited minimal discretization error and were selected for further analysis.

Table 3. Grid independence study.

		Case 1 Model (E-PCM-Ts Placed Only in the Supply Airstream)		Case 2 Model (E-PCM-Ts Placed in All Four Airstreams)	
Mesh Grading	**E-PCM-T Face Element Size [mm]**	**Nodes**	**Elements**	**Nodes**	**Elements**
Fine	10	2,207,331	11,684,429	2,899,882	14,512,606
Medium	12	1,276,807	7,141,564	1,969,358	9,969,741
Coarse	15	822,564	4,683,093	1,515,115	7,511,270

2.4.5. Timestep Independence Study

A timestep independence study was conducted to ensure numerical stability and accuracy in the simulation results. This study tested timesteps of 60, 40, 10, and 5 on the selected mesh models. The solution iterated at each timestep and residuals for velocity components, continuity, and energy were monitored until they stabilized with no further variations. The smallest average error was observed with a 5-timestep configuration for velocity outputs, ensuring both accuracy and computational efficiency. Consequently, a 5-timestep configuration was adopted for all simulations.

2.4.6. Boundary Conditions

The inlet air temperature T_{in} at the macroclimate boundary was set to 308.15 K (35 °C), representing a typical outdoor temperature (T_{out}) in hot climatic conditions. The air velocity varied between 1.88 m/s and 3 m/s. To prevent reverse flow, a pressure outlet was positioned at the extended macroclimate domain. The model incorporated a gravitational force of -9.81 m/s^2, while the domain walls were assigned a roughness height of 0.001 Ks. Atmospheric pressure was assumed throughout the simulation. Relaxation factors were set as follows: 0.3 for pressure, 0.7 for momentum, and 1 for energy.

For the E-PCM-Ts, the initial temperature was maintained at 293.15 K (20 °C). A solar fan static pressure jump of 10 Pa was defined. Monitoring points were established along the microclimate ZY plane to collect relevant data, enabling the observation of supply airflow rates, pressure, and temperature. The thermal storage heat transfer of the PCM was analyzed by assessing the liquid fraction (f_l) at 120 flow time intervals.

2.4.7. Solution Convergence

The simulation was conducted with an inlet air velocity of 1.88 m/s at wind angles of 0° and 45°. Supply airflow rates, pressure, and temperature profiles were monitored at all twelve points identified in Figure 7. Additionally, the PCM heat transfer rate was closely observed at 120 s intervals of flow time, with a particular focus on the liquid fraction and average weighted temperature profiles of the PCM. Convergence was achieved when all monitored residuals and properties showed no further changes, ensuring stability and accuracy. Energy conservation was verified to exhibit no errors, confirming the reliability of the solution.

3. Validation of Numerical Method

The validation of the numerical methods was conducted separately for the windcatcher airflow model and the E-PCM-T liquid fraction performance verification model. Both CFD prediction models were compared with experimental data from previous studies [37,55].

3.1. Windcatcher Airflow Model Validation

Before integrating E-PCM-Ts into the windcatcher model, a validation of the windcatcher's airflow performance was carried out. This step ensured the reliability of the CFD model before implementing further modifications. A 1:10 scale model was used for the initial validation, ensuring that its dimensions, boundary conditions, and grids aligned with the experimental setup reported in [37]. The experimental setup in the literature aimed to replicate realistic operating conditions, maintaining a low blockage ratio of 4.8%, which required no corrections. Indoor airflow was measured using a Testo 425 hot-wire anemometer, manufactured by Testo SE & Co. KGaA, located in Titisee-Neustadt, Baden-Württemberg, Germany, with a velocity reading uncertainty between ±0.5% and 1.0%. Pressure coefficients were measured using a DPM ST650 micromanometer with a 166T ellipsoidal Pitot static tube, both manufactured by Dwyer Instruments, Inc. (Michigan City, IN, USA), which provided readings with an uncertainty of ±1.0% and a valid calibration range of ±11°. Smoke visualization tests were conducted to observe airflow patterns, including short-circuiting and vortex formation.

Following successful validation, the model was scaled up to a full-scale (1:1) configuration for a more accurate analysis of the thermal storage performance in the proposed system.

Confidence limits for the average weighted indoor air velocity data from CFD predictions (C_p) were compared against experimental observations (C_o) at 12 monitoring points (Figure 8). Statistical performance was evaluated using three widely recognized metrics [70]. The normalized mean-square error (NMSE) [71] is governed by Equation (15), the Fractional Bias (FB) is governed by Equation (16), and the fraction of predictions within a factor of two observations (FAC2) is governed by Equation (17) [72].

$$\mathrm{NMSE} = \frac{\overline{\left(C_o - C_p\right)^2}}{\overline{C_o C_p}} \tag{15}$$

$$\mathrm{FB} = \frac{\left(\overline{C_o} - \overline{C_p}\right)}{0.5\left(\overline{C_o} + \overline{C_p}\right)} \tag{16}$$

$$\mathrm{FAC2} = \text{fraction of data that satisfies } 0.5 \le \frac{C_p}{C_o} \le 2.0 \tag{17}$$

where "C_o" represents the experiment observations, the data set average is represented by "$\overline{C}$", and "C_p" represents the model predictions.

Results from the windcatcher airflow model validation exercise for the twelve (12) monitored points (P_1–$P_{12\text{-exhaust}}$) are presented in Table 4. High airflow rates at 0.47 m/s, 1.19 m/s, and 2.82 m/s were observed at P_7, $P_{10\text{-bottom}}$, and $P_{11\text{-supply}}$ in the CFD predictions compared to in the experimental observations, as shown in Figure 9. However, the maximum percentage deviation occurred at P_8 at 32%. P_2 and P_6 exhibited the least deviation at 0%. As highlighted in Figure 10, the overall average percentage error between the CFD predictions and the observations was 3% for the NMSE, 12% when the FB method was used, and an average value of 1.07 for the FAC2 method.

The slight discrepancies seen between the airflow behavior in the CFD results and the experimental data in points 3, 5, 7, 10-bottom, and 11-supply may be attributed to the differences in some of the boundary condition assumptions, which may have influenced the airflow pattern prediction in the model. Additionally, the effect of re-scaling the model caused a slight mismatch in the Reynolds numbers and thermal characteristics within the model. However, overall, validation results indicate that the confidence limits and accuracy of the CFD airflow model predictions are in strong correlation with [37].

Table 4. Average weighted velocities and errors at monitor points P_1–$P_{12\text{-exhaust}}$ for CFD predictions and experimental observations data from the literature.

Monitor Points	P_1	P_2	P_3	P_4	P_5	P_6	P_7	P_8	P_9	$P_{10\text{-bottom}}$	$P_{11\text{-supply}}$	$P_{12\text{-exhaust}}$
V for C_o [m/s]	0.29	0.22	0.28	0.25	1.05	0.22	0.23	0.28	0.29	0.81	2.51	0.30
V for $C_{p(L)}$ [m/s]	0.30	0.20	0.30	0.31	1.08	0.21	0.22	0.29	0.29	0.79	2.50	0.32
V for C_p [m/s]	0.32	0.21	0.17	0.30	1.19	0.21	0.47	0.16	0.27	1.19	2.82	0.37
D%	1	0	28	4	1	0	22	32	1	15	1	4
FAC2	1.12	0.93	0.59	1.21	1.13	0.96	1.60	0.57	0.92	1.47	1.12	1.23
Average FAC2												1.07
NMSE												3%
FB												12%

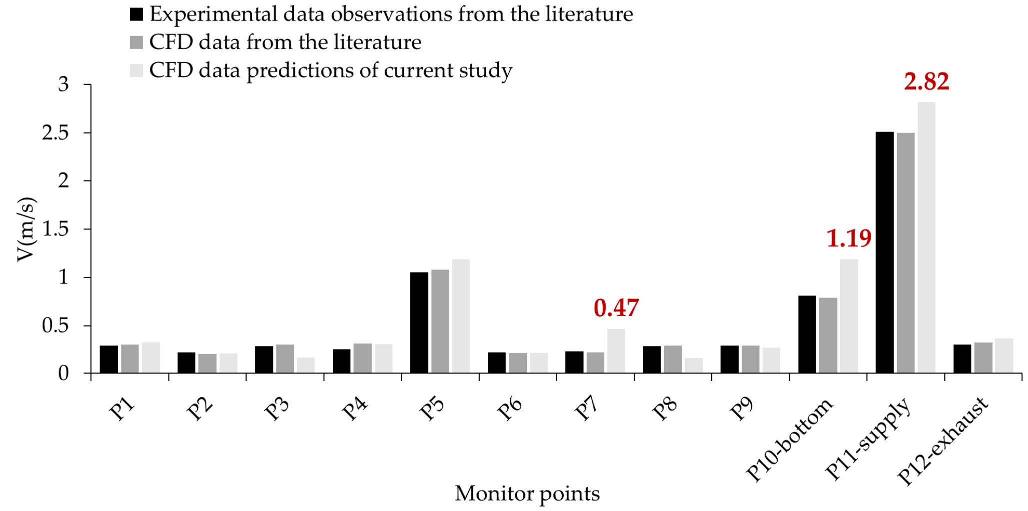

Figure 9. Comparison of indoor velocity CFD and experimental observation data showing C_p having the highest air flow discrepancy values at P_7, $P_{10,}$ and $P_{11\text{-supply}}$.

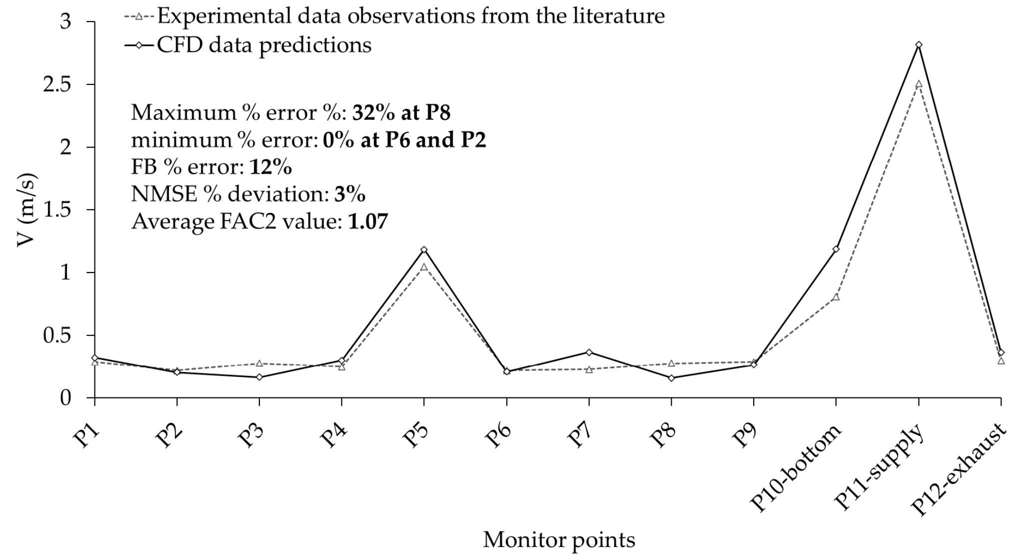

Figure 10. Comparison of indoor velocity CFD predictions (C_p) and experimental observation C_o data at P_1–$P_{12\text{-exhaust}}$ at 3 m/s outdoor wind speed showing the % deviation values.

3.2. E-PCM-T Liquid Fraction Model Validation

The validation of the E-PCM-T model involved comparing the spatial average liquid fraction per-flow rate in the CFD predictions of three different E-PCM-T models with the experimental observations in Rouault et al.'s study [55] under similar boundary conditions. The experiment was set up by placing aluminum-encapsulated PCM tubes inside an energy storage unit. This unit consisted of 42 horizontally layered PCM-filled aluminum tubes arranged parallel to each other within a wooden casing. As described in [55], thermocouples were installed in the storage unit to measure temperature variations during the experiment, facilitating heat transfer analysis. External heat transfer was also maintained at zero during the measurements to align the experimental measurements better with the simulation results. A temperature measurement error of ±0.7 °C was adopted at the inlet, with an overall measurement uncertainty of 1.5%.

To validate the CFD model with the experimental data, $C_{o(E)}$, the CFD predictions, C_p, of the PCM liquid fraction, f_l, and the temperature variation, ΔT, in the encapsulation material (aluminum tube) during the PCM phase change in this study were monitored for 600 min of simulation time. The C_p of f_l in the current study was compared with $C_{o(E)}$ and $C_{o(N)}$ from Rouault et al.'s study [58], as shown in Figure 11. Figure 12 illustrates the variation in the C_p of the encapsulation tube temperature T_t in the current study compared to the $C_{o(E)}$ and $C_{o(N)}$ from Rouault et al.'s study [55]. The maximum deviation in tube temperature, T_t, between $Co_{(E)}$ and C_p was approximately 2.048. Despite this slight deviation, the CFD model effectively validated its accuracy in simulating this aspect of heat transfer, particularly for tube temperatures.

As indicated in Table 5, the NSME statistical calculation reveals a 4.15% and 0.03% deviation from the experimental observations for f_l and the air temperature T. However, no deviation was observed in T_t. The FB deviation percentage was 4.76%, 0.52%, and 1.64% for the models of f_l, T_t, and T, respectively. Using FAC2, the deviation was at 1.20, 1.00, and 1.00 for the same monitored properties, respectively. Meanwhile, the maximum deviation values between $C_{o(E)}$ in the literature and C_p in the current study were 0.29, 2.05, and 6.64, respectively. The deviation in T was the most significant of all properties measured.

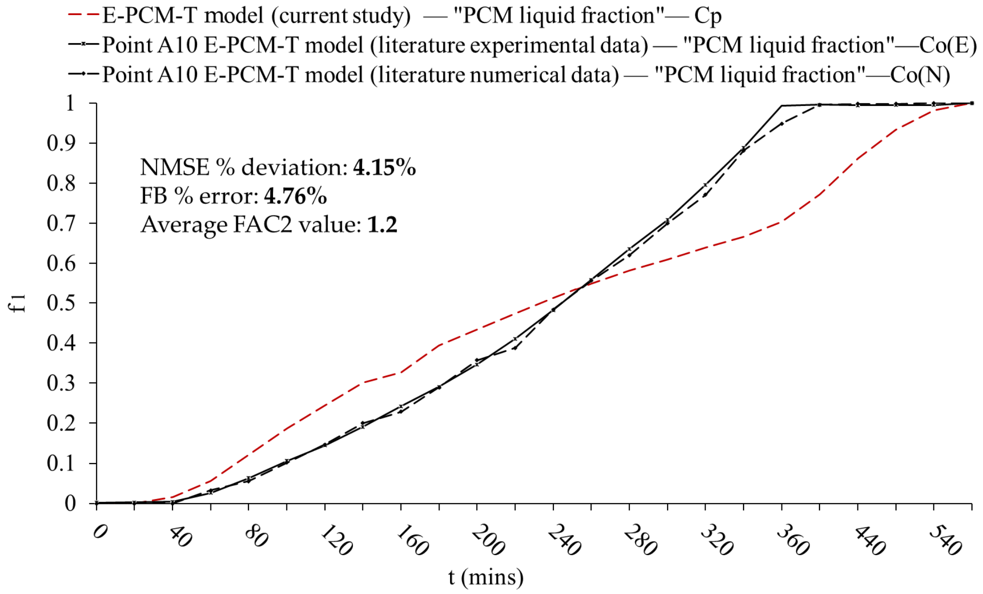

Figure 11. Validation of E-PCM-T model—comparison of PCM liquid fraction CFD predictions, C_p, in the current study; experimental observations, $C_{o(E)}$, from the literature; and CFD predictions, $C_{o(N)}$, in the literature.

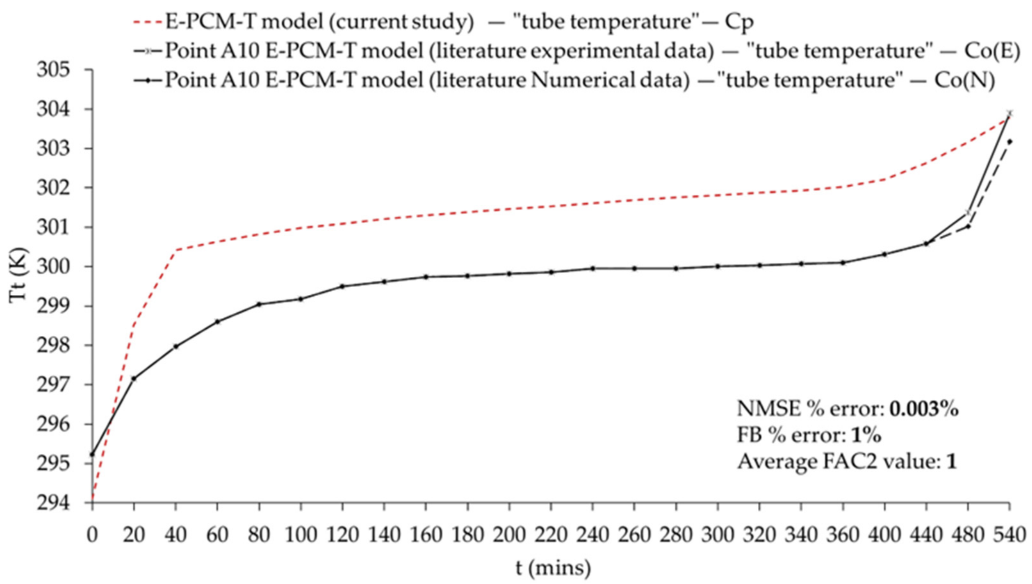

Figure 12. Validation of E-PCM-T model—comparison of tube temperature CFD predictions, C_p, in the current study; experimental observations, $C_{o(E)}$, from the literature; and CFD predictions, $C_{o(N)}$, in the literature.

Table 5. Values of NMSE, FB, and FAC2 statistical deviation calculations for PCM liquid fraction, encapsulation tube temperature, and air temperature.

	NMSE (%)	FB (%)	FAC2	Maximum Deviation Value Between $C_{o(E)}$ and C_p
PCM liquid fraction	4.15	4.76	1.20	0.29
Encapsulation tube temperature (k)	0.00	0.52	1.00	2.05
air temperature (k)	0.03	1.64	1.00	6.64

There were slight differences in boundary condition assumptions due to the scaling factor applied in the CFD model. However, the temperature variation trend over time closely aligned with the expected heat transfer behavior, which was the primary focus of the validation process. As a result, the emphasis was placed on the relative changes in temperature rather than the exact initial temperature values. Nonetheless, the C_p value of the E-PCM-T model showed strong agreement with data from the literature, further reinforcing the validity of the model.

4. Results and Discussion

4.1. Ventilation Performance Assessment

This section presents the results of the numerical analysis of ventilation performance for the two windcatcher models (Case 1 and Case 2), highlighted in Figure 4. Simulations were conducted under varied inlet wind speeds (V_{in}) at 1.88 m/s and 3 m/s, with the inlet wind angle (V_∞) ranging from 0° to 45°. The impact of solar fan inclusion on ventilation performance was also analyzed.

4.1.1. Impact of Varying Outdoor Wind Speeds on Ventilation Performance

The impact of varying wind speeds on the model's ventilation performance was evaluated, with results indicating that higher wind velocities significantly improved ventilation. For example, as shown in Figure 13a,b, the effect of wind speed variation is visually apparent. The differences in contour grading demonstrate that increasing V_{in} from 1.88 m/s to

3 m/s enhanced airflow velocity through the model, highlighting the direct relationship between wind speed and ventilation efficiency.

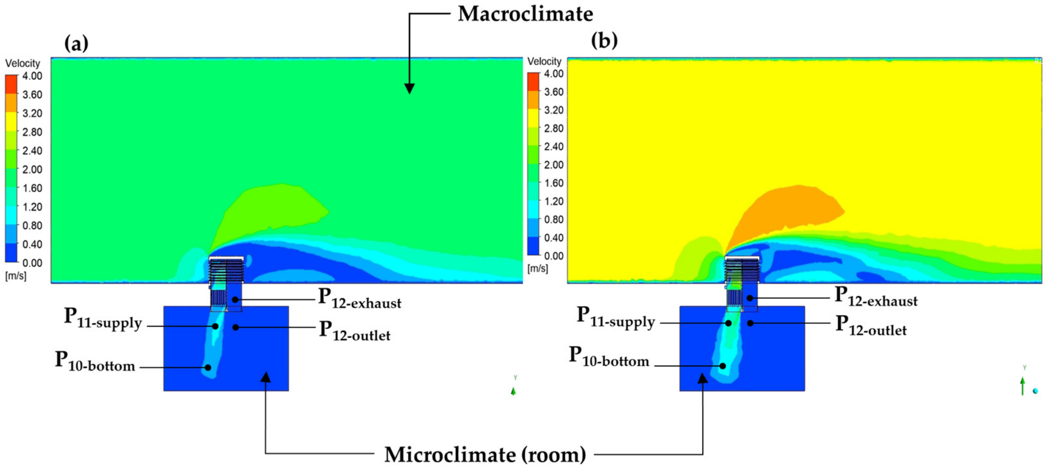

Figure 13. Contour showing the variation in the air velocity magnitude in Case 1 when (**a**) V_{in} is at 1.88 m/s and (**b**) V_{in} is at 3 m/s.

The graphs in Figures 14a,b and 15a,b further highlight in detail the velocity profile at each monitor point. The main increments in air velocity were observed at $P_{11\text{-supply}}$ in both models. However, a 72% increase (from 0.46 m/s to 0.80 m/s) occurred in Case 1 as V_{in} increased from 1.88 m/s to 3 m/s (Figure 14a,b).

Similarly, according to Figure 15a,b, Case 2 exhibited a 69% increase in air velocity at $P_{11\text{-supply}}$ with a velocity increase from 0.37 m/s to 0.61 m/s under the same conditions, though the absolute velocities were lower than those of Case 1.

Figure 16 shows that higher airflow occurred at $P_{11\text{-supply}}$ and near the wall at P_9. This may be due to turbulence in those zones. But airflow dropped significantly at P_2 and P_8, with values ranging from 0.05 to 0.14 m/s and 0.7 to 0.16 m/s when V_{in} was 1.88 m/s and 3 m/s, respectively. This suggests that those regions at P_2 and P_8 could be prone to stagnation of air. Although Case 2 provided better air velocity at eye level (1.5 to 1.7 m from the floor) at $P_{6\text{-mid-supply}}$, with a velocity of 0.42 m/s, Case 1 demonstrated better ventilation performance overall, with V_{in} of 3 m/s delivering more effective airflow.

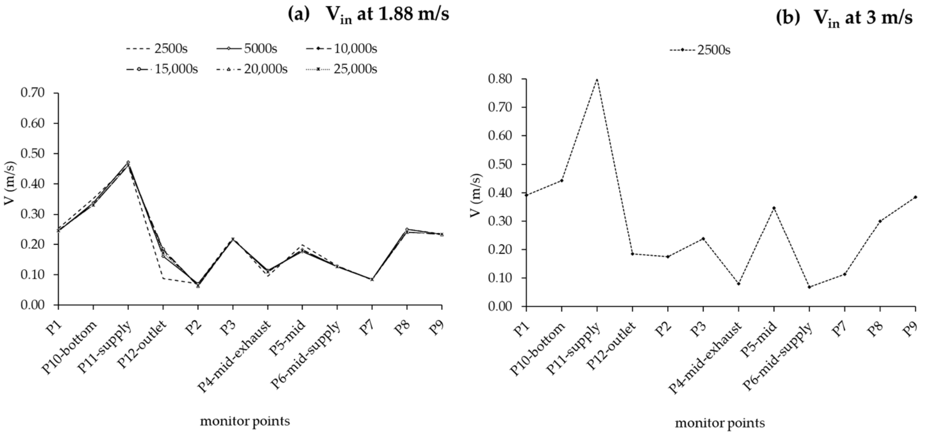

Figure 14. Air velocity profiles for Case 1 when V_∞ is 0° at (**a**) V_{in} 1.88 m/s and (**b**) V_{in} 3 m/s.

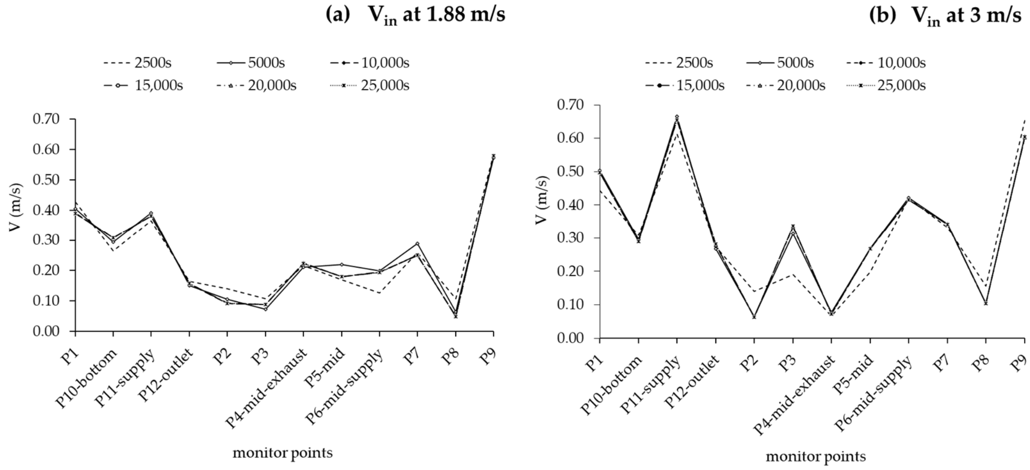

Figure 15. Air velocity profiles for Case 2 when V_∞ is 0° at (**a**) V_{in} 1.88 m/s and (**b**) V_{in} 3 m/s.

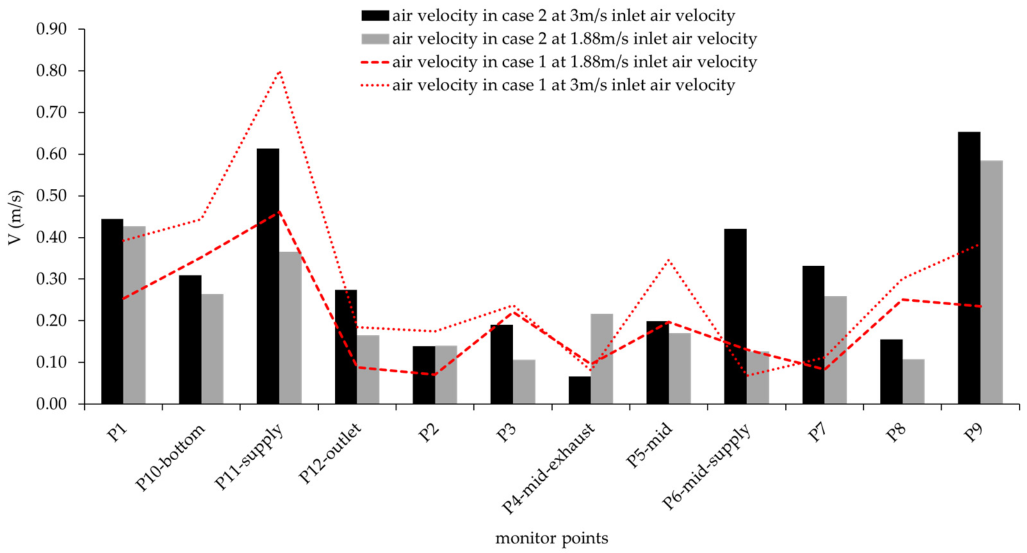

Figure 16. Comparison of air velocity variation in Cases 1 and 2 based on V_{in} 1.88 m/s and 3 m/s scenarios.

Figure 17a,b further compare the air velocity at $P_{11\text{-supply}}$, the base of the room at $P_{10\text{-bottom}}$, and the amount of air exiting the space when V_{in} was at 1.88 m/s. The outlet air velocity was monitored at $P_{12\text{-outlet}}$, located just below $P_{12\text{-exhaust}}$. In both cases, air velocity continued to decrease as air moved from the supply to the base. Case 1 shows better airflow distribution. In Case 1, velocity only decreased from 0.46 m/s at $P_{11\text{-supply}}$ to 0.33 m/s at $P_{10\text{-bottom}}$ and exited at 0.17 m/s (Figure 17a). Case 2 followed a similar trend but with slightly lower values: 0.38 m/s at $P_{11\text{-supply}}$, 0.31 m/s at $P_{10\text{-bottom}}$, and 0.16 m/s at the exit (Figure 17b). The lower airflow in Case 2 is likely due to the placement of E-PCM-T units in both the exhaust and supply airstreams, reducing air movement out of the space.

These results highlight the importance of higher inlet velocities for improving airflow, particularly in areas prone to stagnation. The 3 m/s V_{in} scenario provided better ventilation in both cases, with Case 1 performing more effectively overall.

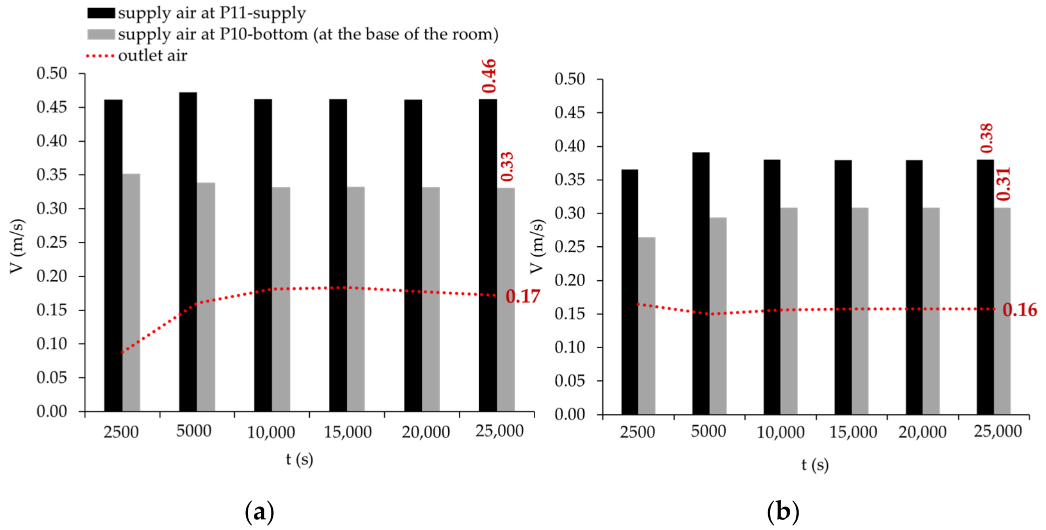

Figure 17. Comparison of air velocities at the supply, base of room, and outlet points when V_{in} is 1.88 m/s for (**a**) Case 1 and (**b**) Case 2.

4.1.2. Impact of Varying Outdoor Wind Angles on Ventilation Performance

The results from the two graphs in Figures 18 and 19 highlight the effect of different wind angle airflow scenarios on the model performance.

Figure 18 compares air velocities at the supply and outlet for wind angles at 0°, 30°, and 45°. At the supply, the 30° wind angle (V_∞) scenario achieved the highest velocity (0.61 m/s), followed by 45° (0.41 m/s) and 0° (0.37 m/s). Similarly, at $P_{12\text{-outlet}}$, the 30° V_∞ scenario recorded the highest outlet air velocity (0.28 m/s), followed by 45° (0.20 m/s) and 0° (0.16 m/s). This shows that 30° offers the best airflow performance. However, a 33% velocity reduction between supply and outlet air was observed in the 30° scenario due to turbulence and energy dissipation, marking the highest decrease among all V_∞ scenarios.

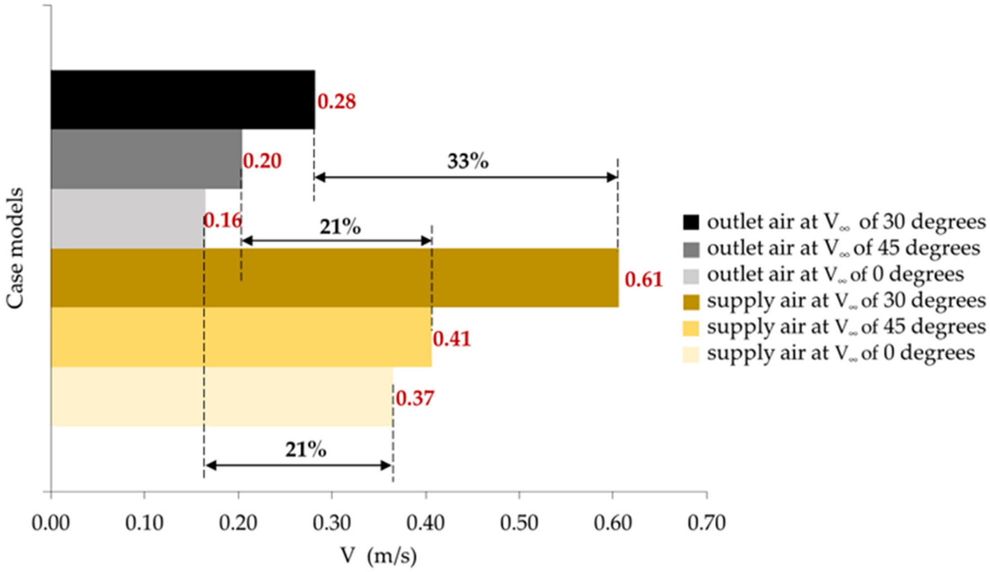

Figure 18. Comparison of the effect of different wind angles V_∞ on the supply and outlet air velocities in the model.

Figure 19 further demonstrates the effectiveness of the 30° V_∞ scenario in enhancing airflow directly at $P_{11\text{-supply}}$. Comparing Cases 1 and 2, the 30° V_∞ scenario in Case 2 achieved the highest velocity (1.11 m/s), representing a 50% improvement in the hybrid ventilation performance compared to the 0° V_∞ scenario (0.61 m/s). The wind angle effect on the windcatcher's ventilation was not as pronounced at V_∞ 0° and 45°, compared to V_∞ at 30°. But V_∞ still impacted the hybrid ventilation performance more in Case 2 than in Case 1. For Case 1, velocities were slightly lower, with minimal differences between the 45° (0.79 m/s) and 0° (0.80 m/s) V_∞ scenarios.

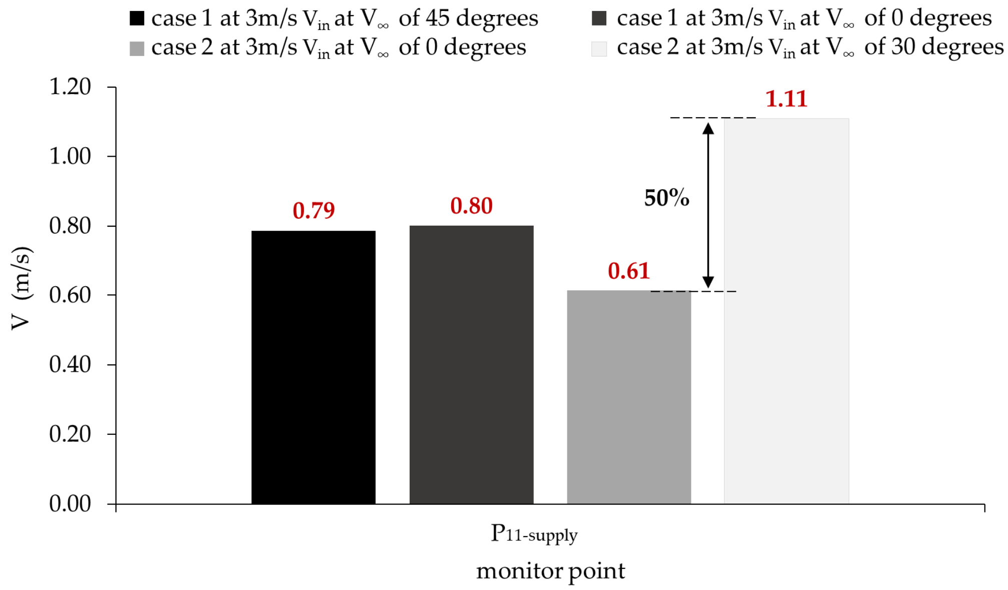

Figure 19. Comparison of the effect of wind angle V_∞ on the solar fan air flow performance of the windcatcher.

These findings emphasize the superior performance of the 30° V_∞ scenario in Case 2, particularly at $P_{11\text{-supply}}$, where it significantly enhances airflow. Overall, the 30° V_∞ scenarios consistently delivered optimal airflow performance by improving air distribution and reducing stagnation. This suggests the importance of wind angles in optimizing air circulation in such systems.

4.1.3. Air Pressure Distribution in the Model

Figure 20 compares air pressure (P) across two case models: Case 1 (V_∞ = 0° and 45°) and Case 2 (V_∞ = 0° and 45°). Case 1a (V_∞ = 0°) recorded the lowest P values, with −0.66 Pa at the supply (P_s) and −0.76 Pa at the exhaust (P_e). P increased with higher wind angles, with Case 1b (V_∞ = 45°) reaching 9.16 Pa at the supply and 9.10 Pa at the exhaust. Case 2b at V_∞ of 45° showed the most balanced air pressure difference, with 8.02 Pa at the supply and 8.00 Pa at the exhaust.

The contours presented in Figure 21 specifically compare the air pressure distribution between Cases 1 and 2 at 7750 s flowtime. From the color gradient seen in the contours presented, it can be inferred that Case 2 indicates a lower air pressure distribution than Case 1.

The graphs in Figure 22a,b present more detailed interpretations of the air pressure difference in the model. Accordingly, a drop in the supply air pressure (P_s) from 3.11 Pa to −0.66 Pa over the first 2500 s is observed (Figure 22a). At the same time, a sharp decrease in the exhaust air pressure (P_e) occurred, from 26.40 Pa to 0.76 Pa, indicating a significant pressure reduction. The pressure drops in Case 2 were more pronounced than in Case 1 (Figure 22b). This sharp drop could be because of high turbulence at the beginning of the simulation or potential air leakages at the supply.

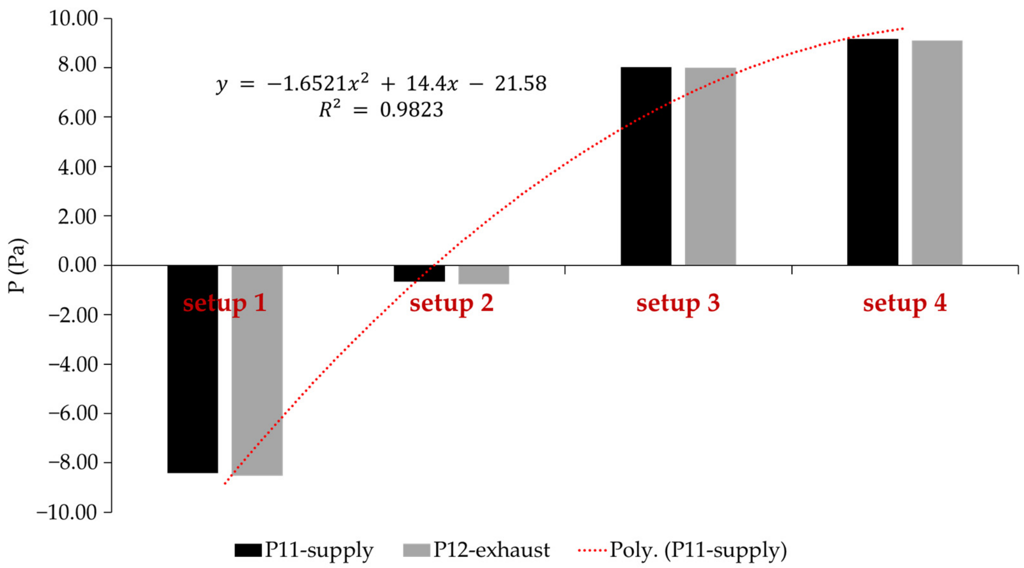

Figure 20. Air pressure comparison across four windcatcher model cases with varying V_∞ at 0° and 45°. Setup 1 represents Case 2 model at V_∞ = 90° and V_{in} = 1.88 m/s. Setup 2 represents Case 1 model at V_∞ = 90° and V_{in} = 1.88 m/s. Setup 3 represents Case 2 model at V_∞ = 45° and V_{in} = 1.88 m/s. Setup 4 represents Case 1 model at V_∞ = 45° and V_{in} = 1.88 m/s.

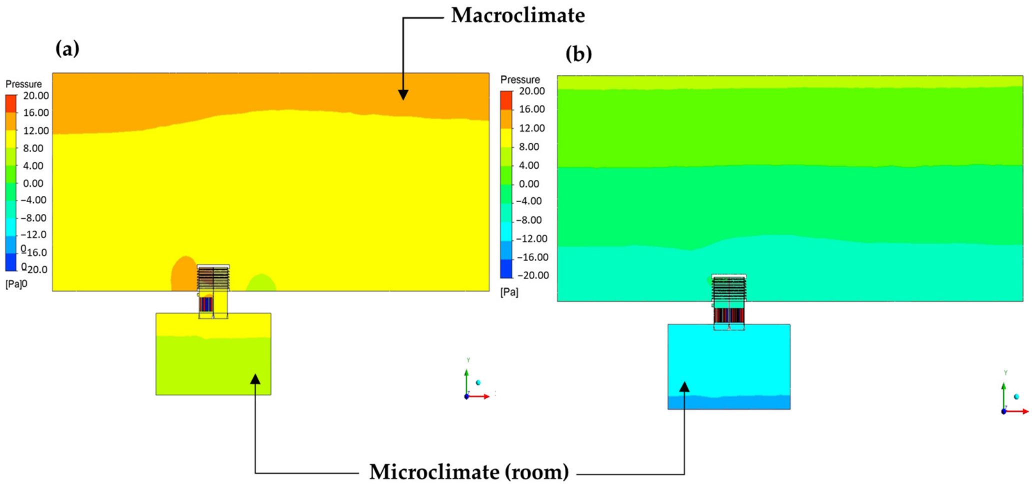

Figure 21. Air pressure contours show a comparison of the air pressure distribution comparison across a ventilated room when V_{in} is at 1.88m/s in (**a**) Case 1 and (**b**) Case 2.

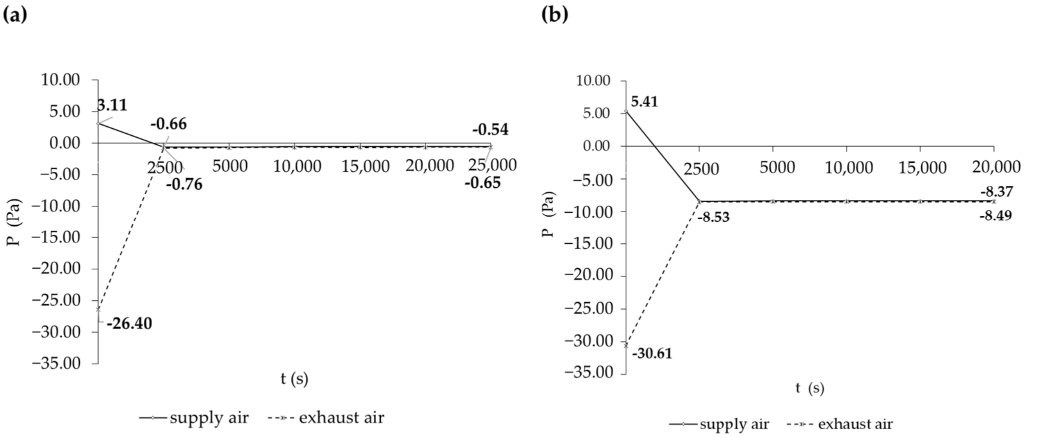

Figure 22. Air pressure P that drops between supply and exhaust air at V_{in} is 1.88 m/s at 0° V_∞: (**a**) Case 1 and (**b**) Case 2.

According to Figure 22b, at the beginning of the simulation, P_e in Case 2 was 30.61 Pa and then dropped to −8.53 Pa after 2500 s, while P_s decreased from 5.42 Pa to −8.41 Pa. A stable air pressure and flow condition was maintained from 2500 s to 25,000 s. By the end of the simulation time at 25,000 s, a positive–negative pressure equilibrium was nearly achieved. This positive–negative pressure equilibrium implies that the ventilation system functioned effectively.

4.2. Cooling Performance Assessment

The cooling performance of the model was assessed at the different V_{in} of 1.88 m/s and 3 m/s. In addition, the effect of different E-PCMT arrangements on system performance at an inlet air temperature (T_{in}) of 308.15 K (35 °C) is presented.

4.2.1. The Impact of Varying Outdoor Wind Speeds on Cooling Performance

Figure 23 displays the air temperature (T) profile for Case 1 and Case 2, recorded at 12 points (P_1–$P_{12\text{-outlet}}$). Results collated after 1.4 h (5000 s simulation time) showed that the highest drops in T occurred at $P_{11\text{-supply}}$. When Vin was 1.88 m/s, $P_{11\text{-supply}}$ dropped to 305.87 K (32.72 °C) and 306.57 K (33.42 °C) when Vin increased to 3 m/s in Case 2. This indicates that more pronounced cooling occurred at lower wind speeds.

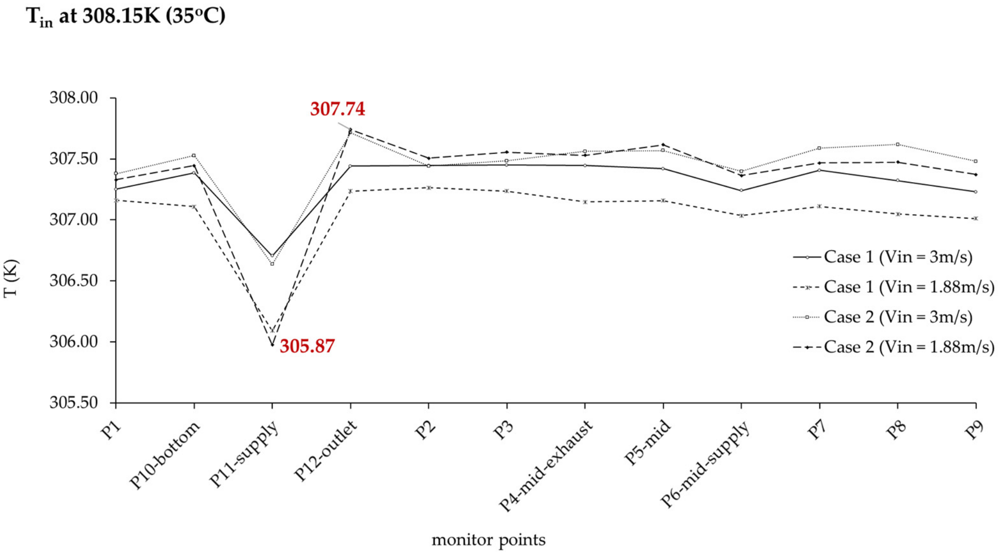

Figure 23. Comparison of air temperature T monitored at P_1–$P_{12\text{-outlet}}$ for Cases 1 and 2 at V_{in} of 1.88 m/s and 3 m/s after 1.4 h of simulation.

At an outdoor inlet air temperature (T_{in}) set at 308.15 K (35 °C), cooling lasted up to 20,000 s of flow time in Case 1 when V_{in} was 1.88 m/s (Figure 24a). From the start of the simulation until 2500 s, a sharp drop in air temperature was observed at $P_{11\text{-supply}}$, followed by a steady decline until 20,000 s, after which the temperature rose sharply again (Figure 24a). As V_{in} increased to 3 m/s (Figure 24b), the sharp temperature rise occurred earlier, at 15,000 s. Temperature drops were more stable at other monitor points (P_1 to $P_{10\text{-bottom}}$) compared to at $P_{11\text{-supply}}$.

Overall, the air temperature values during the effective cooling period ranged between 305.87 K (32.72 °C) in the best-case scenario and 307.30 K (34.15 °C) in the worst-case scenario. The results also indicate that increased wind speed accelerated cooling, achieving faster thermal equilibrium but with reduced duration. In contrast, lower wind speeds sustained a more prolonged cooling period, indicating better temperature stability. The system achieved a maximum air temperature drop of 2.28 °C, representing a 6.51% improvement in cooling at its optimal performance.

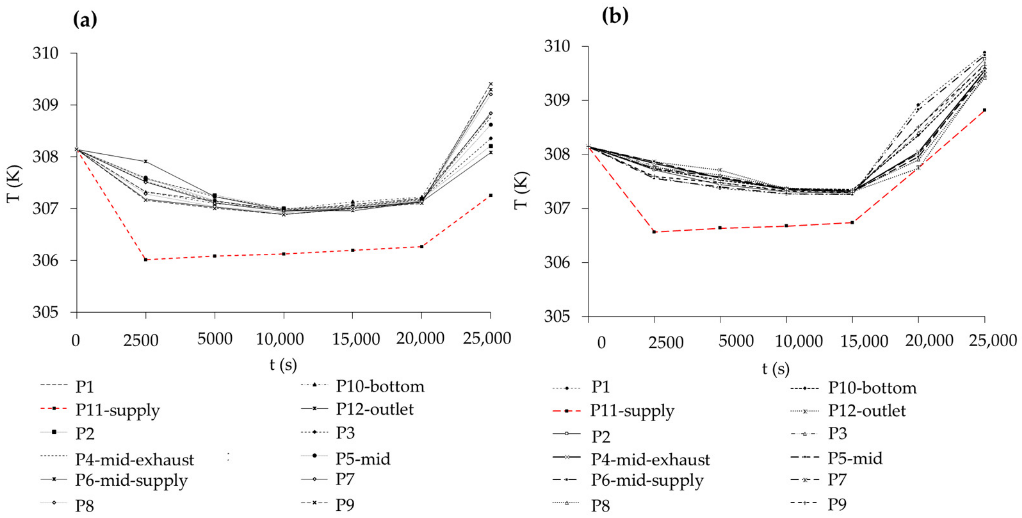

Figure 24. The air temperature T profile throughout the simulation flow time from 0 s to 25,000 s when (**a**) V_{in} is 1.88 m/s and (**b**) V_{in} is 3 m/s in Case 1.

4.2.2. Impact of E-PCMT Arrangement on Cooling Performance

The findings in Figures 25 and 26 highlight the significant influence of the E-PCM-T arrangement on the thermal performance of the system. Figure 25 compares the air temperature contours of Case 1 and Case 2. The contours show a slower but steadily progressive temperature change in the ventilation space in Case 2 compared to in Case 1. At 2500 s, Case 1 achieved a faster temperature reduction and maintained a larger cool zone near the inlet, indicating immediate cooling at the source. However, this effect was short-lived. In contrast, Case 2 exhibited gradual temperature reduction, better regulation, and fewer hot spots, resulting in more balanced cooling over time. The initial cooling advantage in Case 1 was offset by the sustained temperature stability and uniform cooling in Case 2, which persisted throughout the simulation.

As shown in Figure 26a, the optimized E-PCM-T placement in Case 2 improved air–PCM interaction, resulting in a 7% reduction in T_s Compared to Case 1, which achieved only a 6% reduction, Case 2 benefits more from the effectiveness of the E-PCM-T arrangement in maximizing cooling performance.

The improvement in heat transfer dynamics in the exhaust channel in Case 2 is also highlighted in Figure 26b, where a consistent reduction pattern in the T_e profile is observed. This indicates better thermal stability in Case 2 than in Case 1, which exhibited an earlier rise in T_e and less cooling stability over time. By the conclusion of the 25,000 s simulation cycle, Case 2 maintained a T_e of 307.17 K (34.02 °C) compared to the less stable performance of Case 1, which reached 308.09 K (34.94 °C).

Slight temperature non-uniformity and reduced heat transfer at certain points may have resulted from gaps that developed between the PCM and tube wall during phase change, a phenomenon not explicitly captured in this study. Nevertheless, overall, the E-PCM-T arrangements influenced both supply (T_s) and exhaust air (T_e) temperatures. But Case 2 benefited more from the enhanced air–PCM interaction due to its E-PCM-T arrangement in the exhaust airstream.

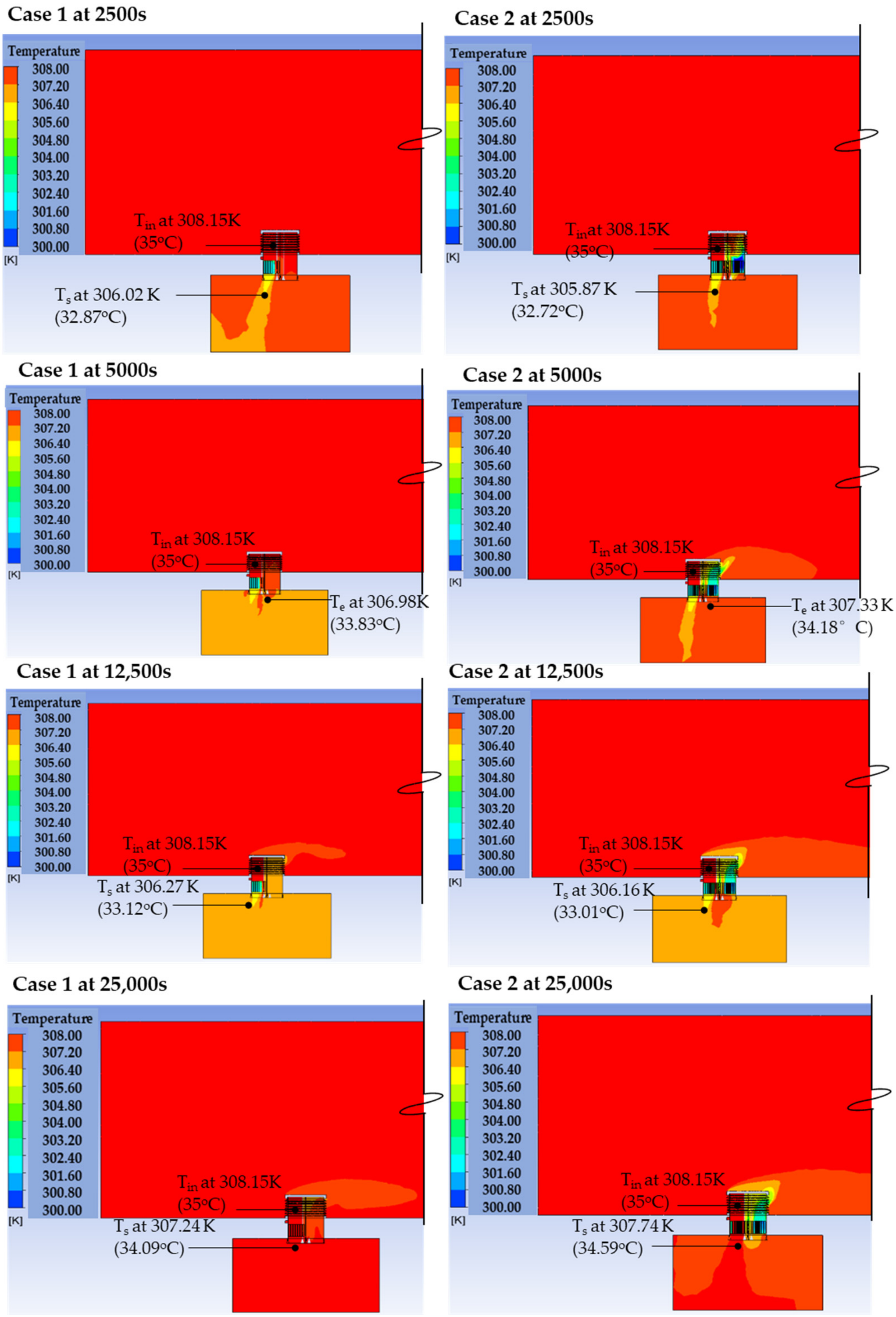

Figure 25. Air temperature contours showing exhaust (T_e) and supply (T_s) temperature variations from 2500 s to 25,000 s based on the inclusion of E-PCM-Ts in the airstreams in Case 1 and Case 2.

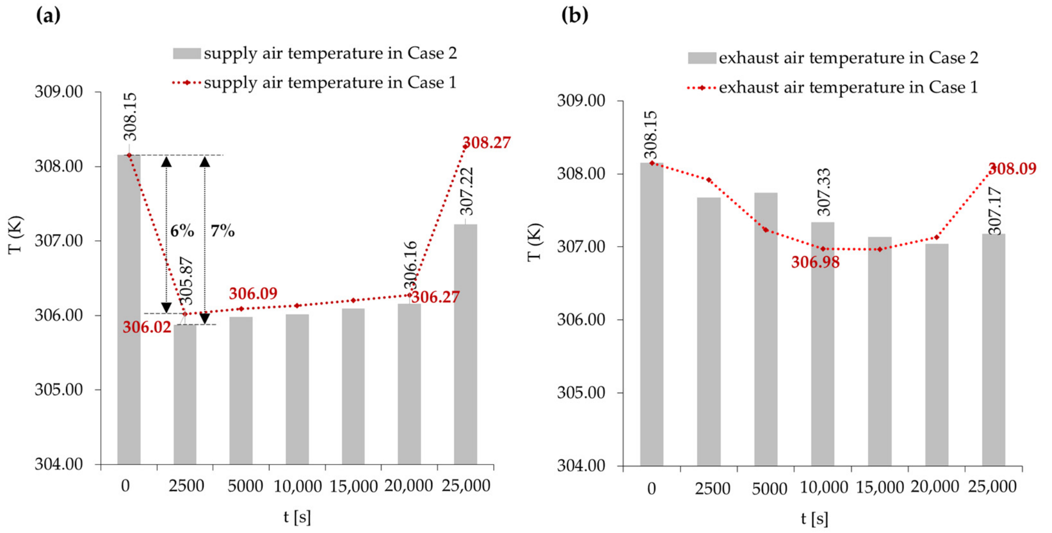

Figure 26. E-PCM-T arrangements' impact on temperatures—(**a**) variation in supply air temperatures T_s for Case 1 and Case 2 and (**b**) variation in exhaust air temperatures, T_e, for Case 1 and Case 2.

4.3. Thermal Energy Storage Performance Assessment

The assessment of the thermal energy storage performance of the model was only based on the charging cycle of the PCM, representing the PCM heat absorption cycle for cooling the incoming air. The effects of variations in wind speeds and E-PCM-T arrangements inside the model are presented in Sections 4.3.1 and 4.3.2.

4.3.1. Impact of Varying Outdoor Wind Speeds on Thermal Energy Storage Performance

Comparing Figure 27a,b, it is observed that the PCM in the E-PCM-Ts in the exhaust air streams discharged faster as V_{in} increased from 1.88 m/s to 3 m/s. However, that of the supply airstream discharged more rapidly in both scenarios.

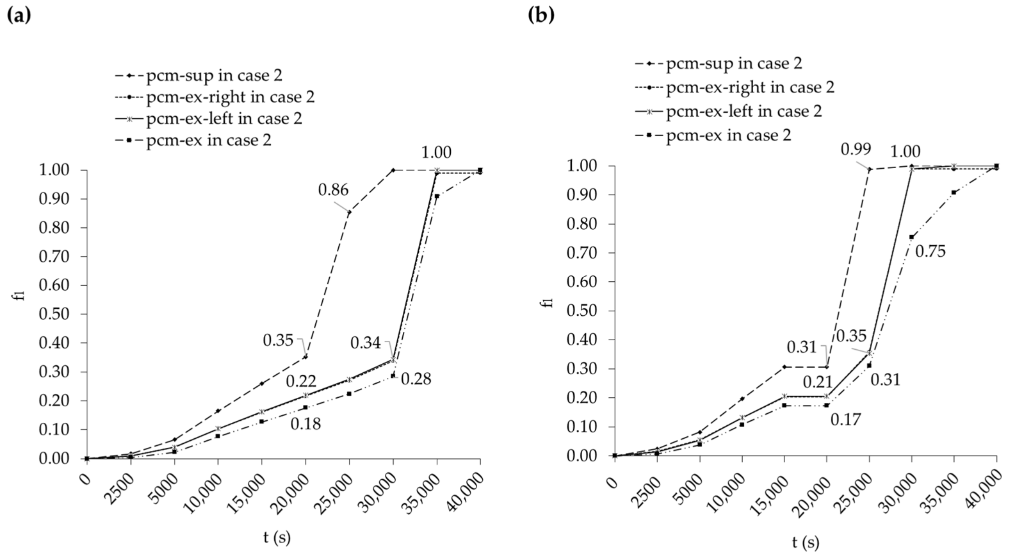

Figure 27. Effect of variation in V_{in} on PCM liquid fraction in Case 2 (**a**) when V_{in} is 1.88 m/s and (**b**) when V_{in} is 3 m/s.

In Case 2, when Vin is 1.88 m/s (Figure 27a), the liquid fraction (f_l) of the PCM in the supply airstream was 0.35 at 20,000 s, while in the other airstreams, f_l was around 0.18. Between 20,000 s and 25,000 s, f_l in the supply airstream sharply increased to 0.89, with complete melting at 30,000 s. In contrast, the PCM in the other airstreams melted more steadily, completing at 35,000 s to 40,000 s.

When V_{in} increases to 3 m/s, the PCM discharging completes faster. As shown in Figure 27b, f_l in the supply airstream was 0.31 at 20,000 s, while in the other airstreams, f_l ranged from 0.21 to 0.17. A sharp rise in f_l occurred between 20,000 s and 25,000 s, reaching 0.99, while the other PCM reached full melting by 30,000 s.

Comparing the results presented in Figure 27a,b, it can be inferred that the improved thermal energy storage performance of the model is achieved at lower V values. In addition, higher wind speeds increase the rate of the PCM discharging, reducing the time required for temperature stabilization.

4.3.2. Impact of E-PCMT Arrangement on Thermal Storage Performance

The impact of the E-PCM-T arrangement on the thermal energy storage performance of Case 1 and Case 2 was studied based on three parameters: PCM discharging cycles, PCM temperature variation, and air temperature stabilization. The liquid fraction contour in Figure 28 shows that from 12,750 s, the PCM in the supply airstream in Case 1 began to melt faster than in Case 2. Although a uniform melting pattern was observed in both cases at 7750 s, PCM melting in the exhaust airstreams occurred in a bottom-up direction after 7750 s and throughout the rest of the simulation. PCM melting in the supply airstreams progressed in the opposite direction to the top-down one. The heat absorption at the base of the PCM in the exhaust airstream in Case 2 improved cooling capacity, leading to better thermal regulation compared to in Case 1.

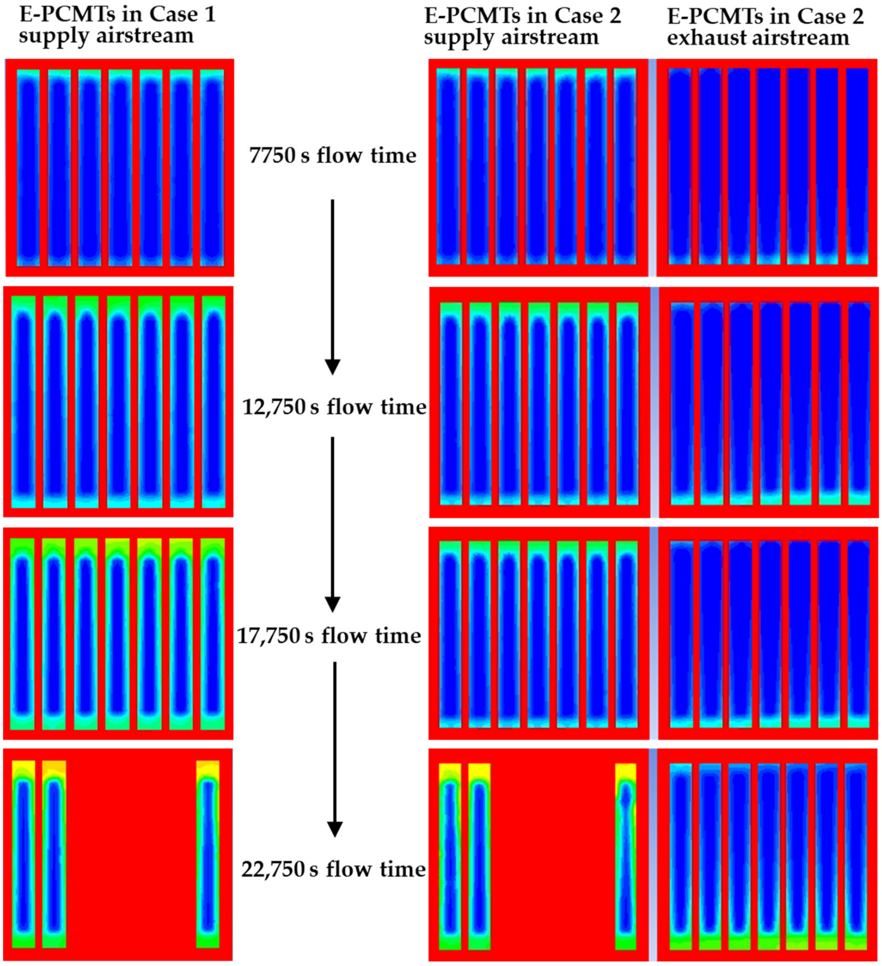

Figure 28. Contour showing PCM liquid fraction comparison between Case 1 and Case 2 based on the E-PCM-T arrangement in supply and exhaust airstreams.

Figure 29a,b compare the PCM charging cycles in Case 1 and Case 2 and their impact on T_s variation. According to Figure 29b, the slower charging cycle in Case 2 delayed sharp temperature increases. As a result, a gradual rise was seen in T_s from 305.87 K (32.72 °C) to 306.16 K (33.01 °C) between 2500 s and 20,000 s at f_l of 0.35. By 25,000 s, T_s rose slightly to 307.77 K (34.62 °C) as the f_l increased to 0.86, confirming relatively stable cooling.

In contrast, Case 1 exhibited faster charging with less thermal stability (Figure 29a). In this case, T_s increased from 306.02 K (32.87 °C) to 306.27 K (33.12 °C) by 20,000 s at a f_l of 0.38, followed by a sharp rise to 308.27 K (35.12 °C) at a f_l of 0.66. The results suggest the potential of the Case 2 configuration to offer better cooling and enhanced temperature stabilization. With such stability ability in windcatcher, there is greater potential for their adaptability in a wider range of indoor environments and conditions.

The PCM temperature T_{pcm} in relation to the E-PCMT arrangement in Case 1 and Case 2 is presented in Figure 30 for the duration of the cooling performance of the model, which took place from 0 to 20,000 s. An increase in T_{pcm} from the initial temperature of 293 K (20 °C) was observed for both Case 1 and Case 2. However, between 10,000 s and 15,000 s, the rate of increase in T_{pcm} in Case 1 superseded that of Case 2 by 0.4%, indicating a 1.1 K temperature difference. Unlike in the Case 1 model, ΔT_{pcm} was gradual in Case 2 throughout the PCM charging cycle up to 20,000 s. The results presented in Figures 29 and 30 imply that the E-PCMT arrangement impacts the duration at which reduced T_s is sustained to achieve stabilized cooling.

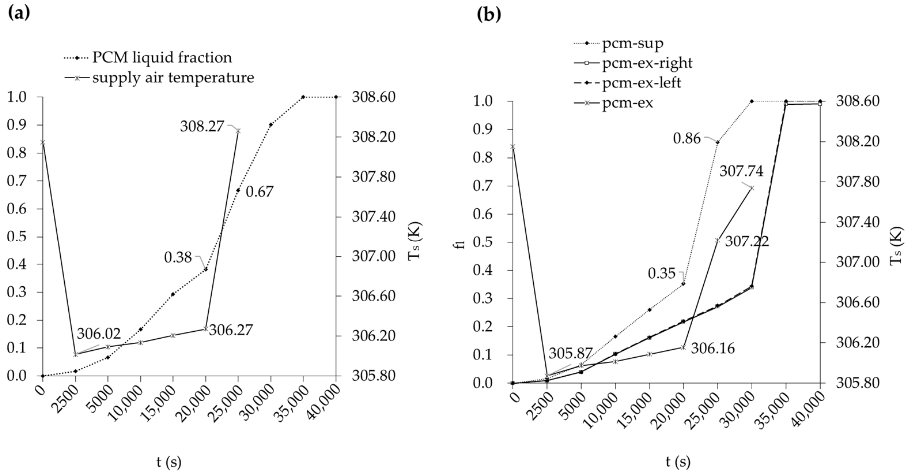

Figure 29. Comparison of supply air temperature T_s and PCM liquid fraction f_l in (**a**) Case 1 and (**b**) Case 2.

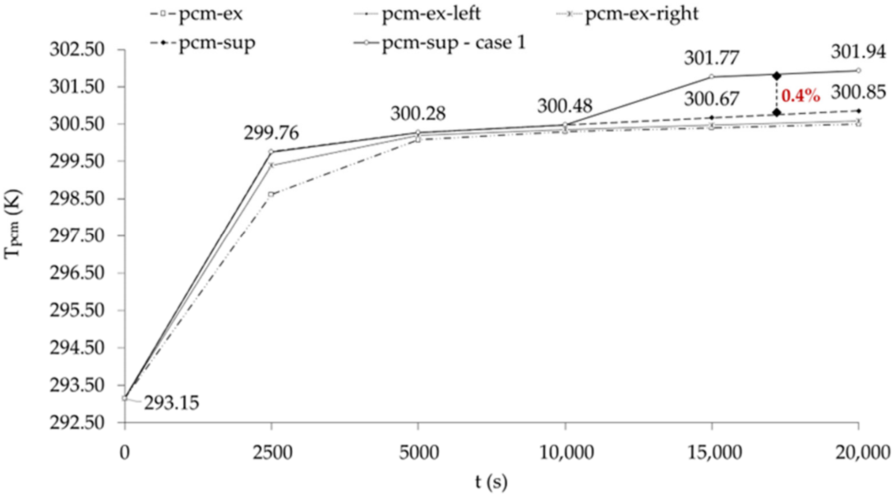

Figure 30. Comparison of PCM temperature T_{pcm} for Case 1 and Case 2.

5. Conclusions

This paper examined the potential of windcatchers and their hybridization for effective ventilation in buildings. Existing studies highlight the challenges of achieving efficient and stable cooling with hybrid multidirectional windcatchers despite their ventilative potential, particularly in hot climates with low wind conditions.

By introducing a solar fan-assisted multidirectional windcatcher integrated with vertically encapsulated PCM tubes (E-PCM-Ts), this research explored an innovative solution to improve the cooling and thermal energy storage performance in such windcatcher systems without compromising ventilation performance. The system's novelty, as discussed in this paper, lies in the vertical integration of E-PCM-Ts within the airstreams, which enhances heat transfer and addresses the temperature stabilization challenges of traditional windcatchers. The use of a wall-mounted solar fan, instead of a roof-mounted one, effectively reduces airflow resistance caused by the PCMs, serving as a consistent secondary airflow vent in addition to the natural ventilation strategy.

Using validated CFD models, this study investigated the effects of wind speeds, angles, and E-PCM-T configurations, leading to the following key findings.

5.1. Ventilation Performance

Higher wind speeds (V_{in}) improved ventilation, with Case 1 achieving a 72% air velocity increase at $P_{11\text{-supply}}$ and Case 2 achieving 69%. Wind angles (V_∞) of 30 ° had the most significant impact, enhancing ventilation by 50%. Adequate hybrid ventilation was achieved with supply air velocities averaging between 0.37 and 0.60 m/s. This hybrid ventilation is especially beneficial for maintaining indoor comfort in low wind conditions, widening the potential application to several building types, particularly in regions with limited wind conditions.

5.2. Cooling Performance

Case 2 demonstrated superior cooling stability, achieving a 6.5% temperature reduction at V_∞ of 0° and Vin of 1.88 m/s. Results showed a maximum air temperature drop of 2.28 °C at a wind speed of 1.88 m/s and wind angle of 0°. Reduced temperatures were sustained for up to 7 h, compared to 4.2–6 h for higher V_{in}. This implies that during peak periods, extended thermal comfort can be achieved, reducing reliance on traditional air conditioning systems.

5.3. Thermal Energy Storage

Lower V_{in} values enhanced PCM performance by prolonging the cooling period. PCM melting was completed by 35,000 s in Case 1 and 30,000–40,000 s in Case 2, depending on wind conditions. The stable temperatures achieved through the prolonged PCM phase-change process minimize indoor temperature fluctuations and reduce the need for frequent active cooling interventions.

Acceptable temperature reduction and stabilization were achieved in the CFD models. However, slight temperature non-uniformity at certain points may have been because of gaps between the PCM and tube wall due to PCM volume expansion during the phase change, which was not accounted for in this study. This possibly may have increased the PCM wall thermal resistance, affecting the heat transfer predictions slightly.

Overall, the findings from this study confirm the potential of PCM-integrated hybrid multidirectional windcatchers to deliver sustainable, energy-efficient cooling and ventilation. Their adaptability to varying wind conditions ensures consistent performance in low wind conditions. As a result, they offer a practical alternative to traditional windcatchers and mechanical cooling systems, making them suitable for diverse building types, including residential, commercial, and institutional applications.

5.4. Future Research

Future research will focus on optimizing the configuration of E-PCM-Ts to further enhance cooling and storage performance. Alternative PCM materials and encapsulation techniques that can improve the system's efficiency and adaptability across diverse climates will be explored. Dynamic meshing will be incorporated, and PCM volume expansion and contraction will be considered in the modeling process to capture these effects and further optimize the model for more accurate results. Exploring the potential for large-scale implementation across various building types would be valuable to deepen the current study further. Hence, economic feasibility studies will be conducted to establish cost-effectiveness. To further assess the scalability and long-term performance of the system, field testing under real-world conditions will also be undertaken. These anticipated future research efforts aim to position the system as a practical and viable ventilative cooling solution for wider building applications.

Author Contributions: Conceptualization, O.E.; methodology, O.E.; software, O.E.; validation, O.E.; formal analysis, O.E.; investigation, O.E.; resources, J.D. and J.C.; data curation, O.E.; writing—original draft preparation, O.E.; writing—review and editing, O.E., J.D. and J.C.; visualization, O.E.; supervision, J.D. and J.C.; project administration, J.D. and J.C.; funding acquisition, O.E. All authors have read and agreed to the published version of the manuscript.

Funding: This research was funded by the Commonwealth Scholarship Commission in the UK under the Commonwealth PhD Scholarship program (Funding Number: NGCS-2019-428).

Data Availability Statement: Data can be made available on request.

Acknowledgments: This work was administratively supported by the Building Energy Environment research group at the Faculty of Engineering, University of Nottingham, UK.

Conflicts of Interest: The authors have no known competing financial interests or personal relationships that could have influenced the work reported in this paper.

Nomenclature

Q	absorbed heat in a room per unit area surface.
T	air temperature
V	air velocity
T_d	daytime room temperature
ρ	density of air
k_{eff}	effective heat conductivity
T_e	exhaust air temperature
V_e	exhaust air velocity
$\overline{C}$	data set average
C_p	CFD model predictions
$C_{1\varepsilon}$	empirical model constant
$C_{2\varepsilon}$	empirical model constant
$C_{3\varepsilon}$	empirical model constant
C_o	experiment observations
P_e	exhaust air pressure
h_i	fluid-specific enthalpy
u	fluid velocity in the model
$\vec{J_i}$	fusion flux of species
g	gravitational acceleration

T_{in}	inlet air temperature
V_∞	inlet wind angle
V_{in}	inlet wind speed
d_i	inner tube dimeter
j_i	mass flux
μ	molecular dynamic viscosity
R_i	net rate of production of species
T_n	nighttime room temperature
$T_{m,r}$	optimal PCM melting temperature
T_{out}	outdoor temperature
d_o	outer tube diameter
t_c	PCM charging time
ρ_{PCM}	PCM density
t_d	PCM discharging time
f_l	PCM liquid fraction
M_{PCM}	PCM mass
T_{pcm}	PCM temperature
ΔT_{pcm}	PCM temperature difference
T_s	PCM temperature at solid
l_f	PCM volume fraction
$V_{PCM,tube}$	PCM volume
D%	percentage deviation at every data point
P	point
p	air pressure
S_i	rate of creating species by addition
s	seconds
$\overline{T}_r$	set average room temperature
S	simulation coefficient
i	species
e	specific internal energy
P_s	supply air pressure
T_s	supply air temperature
V_s	supply air velocity
ΔT	temperature difference
β	thermal expansion coefficient
t	time
G_k	TKE source caused by average velocity gradient
G_b	TKE source based on buoyancy force
T_t	tube temperature
L_t	tube length
H_t	tube height
W_t	tube width
α_k	turbulent Prandtl constant
α_ε	turbulent Prandtl constant
τ_t	turbulence stress divergence due to the velocity fluctuations by the auxiliary stresses

Glossary

AC	Air conditioning
Case 1	Windcatcher model assisted by solar fan with E-PCM-Ts included in only supply airstream
Case 2	Windcatcher model assisted by solar fan with E-PCM-Ts included in all four airstreams
CFD	Computational fluid dynamics
E-PCM-T	Encapsulated phase-change material tubes
GHG	Global greenhouse gas
HVAC	Heating, ventilation, and air conditioning
PCM	Phase-change material

References

1. Li, Y.; Han, M.; Liu, S.; Chen, G. Energy consumption and greenhouse gas emissions by buildings: A multi-scale perspective. *Build. Environ.* **2019**, *151*, 240–250. [CrossRef]
2. Jafari, S.; Kalantar, V. Numerical simulation of natural ventilation with passive cooling by diagonal solar chimneys and windcatcher and water spray system in a hot and dry climate. *Energy Build.* **2022**, *256*, 111714. [CrossRef]
3. Zhong, F.; Calautit, J.K.; Wu, Y. Assessment of HVAC system operational fault impacts and multiple faults interactions under climate change. *Energy* **2022**, *258*, 124762. [CrossRef]
4. Uddin, K.; Saha, B.B. An Overview of Environment-Friendly Refrigerants for Domestic Air Conditioning Applications. *Energies* **2022**, *15*, 8082. [CrossRef]
5. Dong, Y.; Coleman, M.; Miller, S.A. Greenhouse Gas Emissions from Air Conditioning and Refrigeration Service Expansion in Developing Countries. *Annu. Rev. Environ. Resour.* **2021**, *46*, 59–83. [CrossRef]
6. Woods, J.; James, N.; Kozubal, E.; Bonnema, E.; Brief, K.; Voeller, L.; Rivest, J. Humidity's impact on greenhouse gas emissions from air conditioning. *Joule* **2022**, *6*, 726–741. [CrossRef]
7. Calautit, J.K.; O'connor, D.; Tien, P.W.; Wei, S.; Pantua, C.A.J.; Hughes, B. Development of a natural ventilation windcatcher with passive heat recovery wheel for mild-cold climates: CFD and experimental analysis. *Renew. Energy* **2020**, *160*, 465–482. [CrossRef]
8. Rashid, S.A.; Haider, Z.; Hossain, S.M.C.; Memon, K.; Panhwar, F.; Mbogba, M.K.; Hu, P.; Zhao, G. Retrofitting low-cost heating ventilation and air-conditioning systems for energy management in buildings. *Appl. Energy* **2019**, *236*, 648–661. [CrossRef]
9. Nejat, P.; Calautit, J.K.; Fekri, Y.; Sheikhshahrokhdehkordi, M.; Alsaad, H.; Voelker, C. Influence of terrain and atmospheric boundary layer on the ventilation and thermal comfort performance of windcatchers. *J. Build. Eng.* **2023**, *73*, 106791. [CrossRef]
10. Kim, M.K.; Barber, C.; Srebric, J. Traffic noise level predictions for buildings with windows opened for natural ventilation in urban environments. *Sci. Technol. Built Environ.* **2017**, *23*, 726–735. [CrossRef]
11. Prima, Y.; Prima, S. Wind Catcher and Solar Chimney Integrated As An Alternative Ventilation For Urban Dense Settlements In Tropical Climate. *Int. J. Arch. Urban.* **2019**, *3*, 51–68. [CrossRef]
12. Nejat, P.; Jomehzadeh, F. Windcatcher as a Persian sustainable solution for passive cooling. *Civ. Eng. Res. J.* **2018**, *6*, 7. [CrossRef]
13. Bahadori, M.N.; Dehghani-Sanij, A.; Sayigh, A. *Wind Towers*; Springer: Berlin/Heidelberg, Germany, 2016.
14. Arias-Jiménez, N.; Trebilcock-Kelly, M.; Moreno, A.B.; San-Martín, R.F. Wind towers: Potential evaluation of natural ventilation in housing. *Arquiteturarevista* **2021**, *17*, 198–218. [CrossRef]
15. Yazarlou, T.; Barzkar, E. Louver and window position effect on cross-ventilation in a generic isolated building: A CFD approach. *Indoor Built Environ.* **2019**, *31*, 1511–1529. [CrossRef]
16. Li, L.; Mak, C. The assessment of the performance of a windcatcher system using computational fluid dynamics. *Build. Environ.* **2007**, *42*, 1135–1141. [CrossRef]
17. Sangdeh, P.K.; Nasrollahi, N. Windcatchers and their applications in contemporary architecture. *Energy Built Environ.* **2022**, *3*, 56–72. [CrossRef]
18. Pelletier, K.; Calautit, J. Analysis of the performance of an integrated multistage helical coil heat transfer device and passive cooling windcatcher for buildings in hot climates. *J. Build. Eng.* **2022**, *48*, 103899. [CrossRef]
19. Chen, Q. Ventilation performance prediction for buildings: A method overview and recent applications. *Build. Environ.* **2009**, *44*, 848–858. [CrossRef]
20. Li, J.; Calautit, J.K.; Jimenez-Bescos, C. Experiment and numerical investigation of a novel flap fin louver windcatcher for multi-directional natural ventilation and passive technology integration. *Build. Environ.* **2023**, *242*, 110429. [CrossRef]
21. Li, J.; Calautit, J.; Jimenez-Bescos, C. Parametric analysis of a novel rotary scoop dual-channel windcatcher for multi-directional natural ventilation of buildings. *Energy Built Environ.* 2024; *in press*. [CrossRef]
22. Nejat, P.; Fekri, Y.; Sheikhshahrokhdehkordi, M.; Jomehzadeh, F.; Alsaad, H.; Voelker, C. The Windcatcher: A Renewable-Energy-Powered Device for Natural Ventilation—The Impact of Upper Wing Walls. *Energies* **2024**, *17*, 611. [CrossRef]
23. Yang, Y.K.; Kim, M.Y.; Song, Y.W.; Choi, S.H.; Park, J.C. Windcatcher louvers to improve ventilation efficiency. *Energies* **2020**, *13*, 4459. [CrossRef]
24. Zaki, A.; Richards, P.; Sharma, R. The effect of onset turbulent flows on ventilation with a two-sided rooftop windcatcher. *J. Wind. Eng. Ind. Aerodyn.* **2022**, *225*, 104993. [CrossRef]
25. Khakzand, M.; Deljouiee, B.; Chahardoli, S.; Siavashi, M. Radiative cooling ventilation improvement using an integrated system of windcatcher and solar chimney. *J. Build. Eng.* **2024**, *83*, 108409. [CrossRef]
26. Li, J.; Calautit, J.; Jimenez-Bescos, C.; Riffat, S. Experimental and numerical evaluation of a novel dual-channel windcatcher with a rotary scoop for energy-saving technology integration. *Build. Environ.* **2023**, *230*, 110018. [CrossRef]
27. Shayegani, A.; Joklova, V.; Illes, J. Optimizing Windcatcher Designs for Effective Passive Cooling Strategies in Vienna's Urban Environment. *Buildings* **2024**, *14*, 765. [CrossRef]
28. Pakari, A.; Ghani, S. Airflow assessment in a naturally ventilated greenhouse equipped with wind towers: Numerical simulation and wind tunnel experiments. *Energy Build.* **2019**, *199*, 1–11. [CrossRef]

29. Gharakhani, A.; Sediadi, E.; Roshan, M.; Sabzevar, H.B. Experimental study on performance of wind catcher in tropical climate. *ARPN J. Eng. Appl. Sci.* **2017**, *12*, 2551–2555.
30. Calautit, J.K.; Hughes, B.R.; Shahzad, S.S. CFD and wind tunnel study of the performance of a uni-directional wind catcher with heat transfer devices. *Renew. Energy* **2015**, *83*, 85–99. [CrossRef]
31. O'connor, D.; Calautit, J.K.; Hughes, B.R. A novel design of a desiccant rotary wheel for passive ventilation applications. *Appl. Energy* **2016**, *179*, 99–109. [CrossRef]
32. Chohan, A.H.; Awad, J. Wind Catchers: An Element of Passive Ventilation in Hot, Arid and Humid Regions, a Comparative Analysis of Their Design and Function. *Sustainability* **2022**, *14*, 11088. [CrossRef]
33. Dehghani-Sanij, A.; Soltani, M.; Raahemifar, K. A new design of wind tower for passive ventilation in buildings to reduce energy consumption in windy regions. *Renew. Sustain. Energy Rev.* **2015**, *42*, 182–195. [CrossRef]
34. Zhang, B.; Hu, H.; Kikumoto, H.; Ooka, R. Turbulence-induced ventilation of an isolated building: Ventilation route identification using spectral proper orthogonal decomposition. *Build. Environ.* **2022**, *223*, 109471. [CrossRef]
35. Jafari, D.; Shateri, A.; Nadooshan, A.A. Experimental and numerical study of natural ventilation in four-sided wind tower traps. *Energy Equip. Syst.* **2018**, *6*, 167–179.
36. Afshin, M.; Sohankar, A.; Manshadi, M.D.; Esfeh, M.K. An experimental study on the evaluation of natural ventilation performance of a two-sided wind-catcher for various wind angles. *Renew. Energy* **2016**, *85*, 1068–1078. [CrossRef]
37. Calautit, J.K.; Hughes, B.R. Wind tunnel and CFD study of the natural ventilation performance of a commercial multi-directional wind tower. *Build. Environ.* **2014**, *80*, 71–83. [CrossRef]
38. Duan, S.; Jing, C.; Long, E. Transient flows in displacement ventilation enhanced by solar chimney and fan. *Energy Build.* **2015**, *103*, 124–130. [CrossRef]
39. Zhang, H.; Yang, D.; Tam, V.W.; Tao, Y.; Zhang, G.; Setunge, S.; Shi, L. A critical review of combined natural ventilation techniques in sustainable buildings. *Renew. Sustain. Energy Rev.* **2021**, *141*, 110795. [CrossRef]
40. Hughes, B.R.; Calautit, J.K.; Ghani, S.A. The development of commercial wind towers for natural ventilation: A review. *Appl. Energy* **2012**, *92*, 606–627. [CrossRef]
41. Elmualim, A.A. Failure of a control strategy for a hybrid air-conditioning and wind catchers/towers system at Bluewater shopping malls in Kent, UK. *Facilities* **2006**, *24*, 399–411. [CrossRef]
42. Hughes, B.R.; Ghani, S.A. A numerical investigation into the feasibility of a passive-assisted natural ventilation stack device. *Int. J. Sustain. Energy* **2011**, *30*, 193–211. [CrossRef]
43. Lavafpour, Y.; Surat, M. Passive low energy architecture in hot and dry climate. *Aust. J. Basic Appl. Sci.* **2011**, *5*, 757–765.
44. Calautit, J.K.; Hughes, B.R.; Nasir, D.S. Climatic analysis of a passive cooling technology for the built environment in hot countries. *Appl. Energy* **2017**, *186*, 321–335. [CrossRef]
45. Chaudhry, H.N.; Calautit, J.K.; Hughes, B.R. Computational analysis of a wind tower assisted passive cooling technology for the built environment. *J. Build. Eng.* **2015**, *1*, 63–71. [CrossRef]
46. Bouchahm, Y.; Bourbia, F.; Belhamri, A. Performance analysis and improvement of the use of wind tower in hot dry climate. *Renew. Energy* **2011**, *36*, 898–906. [CrossRef]
47. Calautit, J.K.; Chaudhry, H.N.; Hughes, B.R.; Ghani, S.A. Comparison between evaporative cooling and a heat pipe assisted thermal loop for a commercial wind tower in hot and dry climatic conditions. *Appl. Energy* **2013**, *101*, 740–755. [CrossRef]
48. Calautit, J.K.; O'Connor, D.; Sofotasiou, P.; Hughes, B.R. CFD simulation and optimisation of a low energy ventilation and cooling system. *Computation* **2014**, *3*, 128–149. [CrossRef]
49. Liu, L.; Hammami, N.; Trovalet, L.; Bigot, D.; Habas, J.-P.; Malet-Damour, B. Description of phase change materials (PCMs) used in buildings under various climates: A review. *J. Energy Storage* **2022**, *56*, 105760. [CrossRef]
50. Yang, L.; Jin, X.; Zhang, Y.; Du, K. Recent development on heat transfer and various applications of phase-change materials. *J. Clean. Prod.* **2021**, *287*, 124432. [CrossRef]
51. Al-Absi, Z.A.; Hafizal, M.I.M.; Ismail, M.; Mardiana, A.; Ghazali, A. Peak indoor air temperature reduction for buildings in hot-humid climate using phase change materials. *Case Stud. Therm. Eng.* **2020**, *22*, 100762. [CrossRef]
52. O'connor, D.; Calautit, J.K.S.; Hughes, B.R. A review of heat recovery technology for passive ventilation applications. *Renew. Sustain. Energy Rev.* **2016**, *54*, 1481–1493. [CrossRef]
53. Seidabadi, L.; Ghadamian, H.; Aminy, M. A Novel Integration of PCM with Wind-Catcher Skin Material in Order to Increase Heat Transfer Rate. *Int. J. Renew. Energy Dev.* **2019**, *8*, 1–6. [CrossRef]
54. Lizana, J.; De-Borja-Torrejon, M.; Barrios-Padura, A.; Auer, T.; Chacartegui, R. Passive cooling through phase change materials in buildings. A critical study of implementation alternatives. *Appl. Energy* **2019**, *254*, 113658. [CrossRef]
55. Rouault, F.; Bruneau, D.; Sebastian, P.; Lopez, J. Numerical modelling of tube bundle thermal energy storage for free-cooling of buildings. *Appl. Energy* **2013**, *111*, 1099–1106. [CrossRef]
56. Abdo, P.; Huynh, B.P.; Braytee, A.; Taghipour, R. An experimental investigation of the thermal effect due to discharging of phase change material in a room fitted with a windcatcher. *Sustain. Cities Soc.* **2020**, *61*, 102277. [CrossRef]

57. Calautit, J.K.; Aquino, A.I.; Shahzad, S.; Nasir, D.S.; Hughes, B.R. Thermal Comfort and Indoor air Quality Analysis of a Low-energy Cooling Windcatcher. *Energy Procedia* **2017**, *105*, 2865–2870. [CrossRef]
58. Sharshir, S.W.; Joseph, A.; Elsharkawy, M.; Hamada, M.A.; Kandeal, A.; Elkadeem, M.R.; Thakur, A.K.; Ma, Y.; Moustapha, M.E.; Rashad, M.; et al. Thermal energy storage using phase change materials in building applications: A review of the recent development. *Energy Build.* **2023**, *285*, 112908. [CrossRef]
59. Mosaffa, A.; Farshi, L.G.; Ferreira, C.I.; Rosen, M. Energy and exergy evaluation of a multiple-PCM thermal storage unit for free cooling applications. *Renew. Energy* **2014**, *68*, 452–458. [CrossRef]
60. Peippo, K.; Kauranen, P.; Lund, P. A multicomponent PCM wall optimized for passive solar heating. *Energy Build.* **1991**, *17*, 259–270. [CrossRef]
61. Nazir, H.; Batool, M.; Osorio, F.J.B.; Isaza-Ruiz, M.; Xu, X.; Vignarooban, K.; Phelan, P.; Inamuddin; Kannan, A.M. Recent developments in phase change materials for energy storage applications: A review. *Int. J. Heat Mass Transf.* **2019**, *129*, 491–523. [CrossRef]
62. Sheriyev, A.; Memon, S.A.; Adilkhanova, I.; Kim, J. Effect of phase change materials on the thermal performance of res-idential building located in different cities of a tropical rainforest climate zone. *Energies* **2021**, *14*, 2699. [CrossRef]
63. Lei, J.; Yang, J.; Yang, E.-H. Energy performance of building envelopes integrated with phase change materials for cooling load reduction in tropical Singapore. *Appl. Energy* **2016**, *162*, 207–217. [CrossRef]
64. Rubitherm Phase Change Material: PCM RT-line -Versatile Organic PCM for Your Application. Available online: https://www.rubitherm.eu/en/productcategory/organische-pcm-rt (accessed on 1 February 2025).
65. Dinker, A.; Agarwal, M.; Agarwal, G. Heat storage materials, geometry and applications: A review. *J. Energy Inst.* **2017**, *90*, 1–11. [CrossRef]
66. Rodríguez-Vázquez, M.; Hernández-Pérez, I.; Xamán, J.; Chávez, Y.; Gijón-Rivera, M.; Belman-Flores, J.M. Coupling building energy simulation and computational fluid dynamics: An overview. *J. Build. Phys.* **2020**, *44*, 137–180. [CrossRef]
67. Prakash, S.A.; Hariharan, C.; Arivazhagan, R.; Sheeja, R.; Raj, V.A.A.; Velraj, R. Review on numerical algorithms for melting and solidification studies and their implementation in general purpose computational fluid dynamic software. *J. Energy Storage* **2021**, *36*, 102341. [CrossRef]
68. Hu, Z.; Xue, D.; Wang, W.; Tian, H.; Yin, Q.; Xuan, Y.; Chen, D. Numerical investigation of the melting characteristics of spherical-encapsulated phase change materials with composite metal fins. *J. Energy Storage* **2023**, *68*, 107902. [CrossRef]
69. Franke, J.; Hellsten, A.; Schlunzen, K.H.; Carissimo, B. The COST 732 Best Practice Guideline for CFD simulation of flows in the urban environment: A summary. *Int. J. Environ. Pollut.* **2011**, *44*, 419. [CrossRef]
70. *Designation D 6589-00*; Standard Guide for Statistical Evaluation of Atmospheric Dispersion Model Performance. American Society for Testing and Materials: West Conshohocken, PA, USA, 2000.
71. Hanna, S.; Strimaitis, D.; Chang, J. *Hazard Response Modeling Uncertainty (a Quantitative Method). Volume 1. User's Guide for software for Evaluating Hazardous Gas Dispersion Models*; Final Report, April 1989–April 1991; Sigma Research Corp.: Westford, MA, USA, 2023.
72. Chang, J.C.; Hanna, S.R. Air Quality Model Performance Evaluation. *Meteorol. Atmos. Phys.* **2004**, *87*, 167–196. [CrossRef]